

Investigating ChaMPlane X-ray sources in the Galactic Bulge with Magellan LDSS2 spectra

Xavier Koenig,¹ Jonathan E. Grindlay,¹ Maureen van den Berg,¹ Silas Laycock,¹ Ping Zhao,¹ JaeSub Hong¹ and Eric M. Schlegel²

ABSTRACT

We have carried out optical and X-ray spectral analyses on a sample of 136 candidate optical counterparts of X-ray sources found in five Galactic-bulge fields included in our *Chandra* Multi-wavelength Plane Survey. We use a combination of optical spectral fitting and quantile X-ray analysis to obtain the hydrogen column density towards each object, and a three-dimensional dust model of the Galaxy to estimate the most probable distance in each case. We present the discovery of a population of stellar coronal emission sources, likely consisting of pre-main sequence, young main sequence and main sequence stars, as well as a component of active binaries of RS CVn or BY Dra type. We identify one candidate quiescent low-mass X-ray binary with a sub-giant companion; we note that this object may also be an RS CVn system. We report the discovery of three new X-ray detected cataclysmic variables (CVs) in the direction of the Galactic Center (at distances $\lesssim 2$ kpc). This number is in excess of predictions made with a simple CV model based on a local CV space density of $\lesssim 10^{-5}$ pc $^{-3}$, and a scale height ~ 200 pc. We discuss several possible reasons for this observed excess.

Subject headings: surveys — stars: activity — stars: late type — Galaxy: stellar content — novae, cataclysmic variables — X-rays: stars

1. Introduction

The goal of the *Chandra* Multi-wavelength Plane Survey (ChaMPlane)¹ is to study the galactic X-ray point-source population, in particular accretion-powered X-ray sources.

¹Harvard-Smithsonian Center for Astrophysics, 60 Garden Street, Cambridge, MA 02138; xkoenig@cfa.harvard.edu

²Department of Physics and Astronomy, University of Texas at San Antonio, 1 UTSA Circle, San Antonio, TX 78249

¹<http://hea-www.harvard.edu/ChaMPlane>

ChaMPlane (24; 25) comprises two phases of study of the Galactic plane (Galactic latitudes $|b| < 12^\circ$): firstly an X-ray survey of serendipitous sources from archival deep *Chandra* X-ray Observatory pointings (with exposure times greater than ~ 20 ks), and secondly an optical survey in $H\alpha$ (narrow band) and Johnson V , R , and I filters, using the Mosaic camera on the CTIO and KPNO 4m telescopes to image $36' \times 36'$ fields centered on the *Chandra* pointings. Optical spectra are then obtained for classification of candidate optical counterparts to X-ray sources. Infrared (IR) observations are used to identify candidate counterparts in heavily obscured fields.

In this paper we analyze a sample of candidate optical counterparts from five ChaMPlane fields towards the Galactic bulge using low-resolution optical spectra. These fields are within 20° of the Galactic Center (GC), and within 3° of the Galactic plane. Using the optical band necessarily constrains the scope of this project: stars at the distance of the GC (~ 8 kpc) are hidden behind a hydrogen column density $N_H \sim 0.5\text{--}2.0 \times 10^{23} \text{ cm}^{-2}$, and are thus absorbed by $A_V \gtrsim 25$ ($A_R \gtrsim 19$). Given our optical survey limit of $R = 24$ and this level of extinction, optical counterparts at the GC are unobservable, therefore our work is restricted to foreground ($d \lesssim 3$ kpc) sources. As a consequence we focus our efforts on two main goals: 1) to identify candidate cataclysmic variables (CVs) through their broad $H\alpha$ line emission and 2) to study the properties of the sample of stellar coronal emission sources that we detect. In doing so we highlight anomalous cases as potential active binary or quiescent low-mass X-ray binary (qLMXB) systems.

The X-ray and optical datasets used in this study, and their reduction, are discussed in §2–3. In §3 we highlight new techniques developed for our analysis—a simple spectral fitting process to obtain the extinction $E(B - V)$ and thus N_H from the optical spectra, a three-dimensional (3D) dust model of the Galaxy (17) to obtain a distance in any direction given $E(B - V)$, and the X-ray Quantile Color-Color Diagram (QCCD) technique for spectral analysis of low-count X-ray point sources. In §4 we give results for X-ray and optical source properties and present our detected candidate CVs and observed stellar X-ray luminosity function. In §5 we discuss the likely composition of our stellar coronal source population and compare the CV sample to predictions of a simple Galactic distribution model. Finally in §6 we present our conclusions.

2. Observations and Datasets

2.1. X-ray Dataset

Hong et al. (29) and Hong et al. (2008, in preparation) describe in detail our pipeline

processing of archival *Chandra* observations for use in the ChaMPlane survey and subsequent, more detailed analysis. In summary, source lists from detections in a broad (B_X , 0.3–8.0 keV), soft (S_X , 0.3–2.5 keV) and hard (H_X , 2.5–8.0 keV) energy band, are cross-correlated to form a master source list. Source properties such as flux and energy quantiles (see §3.1), are derived in energy bands more appropriate to analysis of low count sources. These conventional bands are defined: S_C (0.5–2.0 keV), H_C (2.0–8.0 keV) and B_C (0.5–8.0 keV). In the following analysis, we consider only X-ray sources of level 1 and above—these being sources unaffected by hot pixels, bad columns or bad bias values on the ACIS detector, or readout streaks from bright sources as well as sources too close to the chip boundary; see Hong et al. (29) for a complete description of the different levels assigned to sources in our X-ray catalog.

X-ray data for this paper come from three ACIS-I and one ACIS-S *Chandra* pointings. In addition, we have stacked 14 ACIS-I observations centered on SgrA* to create a deep image of the Galactic Center region. This stack includes the observations analyzed by Muno et al. (40) (with the exception of ObsID 1561), that amount to a total of 590 ksec exposure time, as well as ObsIDs 3549, 4683, 4684 and 5360. The resultant total exposure time is 748ks or 698ks of good time after processing. The process of dealing with duplicate sources between individual pointings in the stack is detailed in Hong et al. (29). The final stacked SgrA* observation we label ObsID 53392. It overlaps partially with ObsID 945—the two share 46 X-ray sources in common. All fields listed in Table 1 were observed with *Chandra* ACIS-I except J1655, for which ACIS-S was used. Exposure times are given before and after correcting for good time intervals (GTI).

Table 1. X-ray Observations used in this Paper

| Obs. ID | Field Name | Aimpoint | | No. of Sources ^a B_X | Exposure (ks) | Effective exp. (ks) | N_{22} (cm^{-2}) ^b |
|--------------------|-------------------------|---------------|---------------|--------------------------------------|------------------|------------------------|---|
| | | $l(^{\circ})$ | $b(^{\circ})$ | | | | |
| 99 | GRO J1655–40 (J1655) | 344.98178 | 2.45612 | 137 | 43.0 | 42.3 | 1.0 |
| 737 | G347.5–0.5b (G347b) | 347.36606 | –0.85734 | 108 | 40.0 | 38.2 | 3.3 |
| 944 | SgrB2 | 0.58834 | –0.02491 | 369 | 100.0 | 96.8 | 10.8 |
| 945 | Gal. Center Arc (GalCA) | 0.14055 | –0.09707 | 222 | 50.0 | 48.5 | 10.8 |
| 53392 ^c | SgrA* | 359.94415 | –0.04594 | 2982 | 748.0 | 698.0 | 4.3 |

^aNumber of valid (level 1) sources found in the B_X band.

^bIntegrated column density N_H in units of 10^{22} up to a distance of 8 kpc, from Drimmel & Spergel (17).

^cObsID 53392 is a number we assign internally to refer to our stacked SgrA* observation.

2.2. Optical Dataset

Targets for optical spectral follow-up were selected following observations made in March 2000 with the Mosaic camera on the CTIO 4m telescope in V , R , I and $H\alpha$ filters to identify candidate counterparts as follows (see 70, for details). We determine the systematic offsets between the Chandra and Mosaic astrometries, i.e. the boresight correction, for each pair of X-ray and optical images using the iterative procedure described in Zhao et al. (70). After applying the boresight correction, we search for candidate optical counterparts within some confidence radius of each X-ray source, taking into account optical and X-ray astrometric uncertainties and the boresight error. We elected to search within a 2σ radius of each source (thus losing on average $\sim 5\%$ of the real counterparts). Table 2 summarizes these results. The resultant catalog of candidate counterparts was used to make a target list for the observing runs in 2001–2002 with the Low Dispersion Survey Spectrograph 2 (LDSS2) on the 6.5m Baade Magellan telescope.

The LDSS2 instrument² uses a multi-aperture mask with a $\sim 5'$ diameter field of view. With a dispersion of 5.3\AA per pixel, we obtained spectra centered on 6500\AA covering ~ 3500 to 9500\AA at a resolution of 13.3\AA . Masks for LDSS2 were generated with the *ldss2mask.f* FORTRAN code. Using slit lengths between ~ 5 and $10''$, and 3 or 4 alignment stars, between 6 and ~ 20 targets were assigned to each mask. Given the ChaMPlane goal of finding X-ray binaries largely powered by accretion processes, highest priority for inclusion of targets on the masks went to objects showing both X-ray and $H\alpha$ emission (i.e. $H\alpha - R < -0.3$), followed by X-ray source candidate optical counterparts (regardless of X-ray or optical colors), then $H\alpha$ bright objects ($H\alpha - R < -0.3$), and then ‘marginal’ $H\alpha$ objects (with $-0.3 < H\alpha - R < -0.2$). Each of these groups was sorted in order of R-magnitude brightness, with brightest objects having highest priority. Details of the observations are given in Table 3.

Data from LDSS2 were reduced using the standard IRAF procedure *ccdproc*. Spectra were extracted one-by-one using the IRAF *doslit* package. When crowding in dense fields resulted in multiple stars falling on a slit, the correct target star was identified for extraction by comparing the dispersed CCD image of the spectra with the Mosaic image of the field and a reference image of the sky taken without the LDSS2 slit mask and grism in place. Stars too poorly exposed to find any trace on the CCD, too badly saturated, or on incorrectly cut slits were not extracted (these three cases account for $\sim 20\%$ of the original targets). In total we extracted 136 usable targets within the five *Chandra* fields-of-view. Flux calibration was performed on each extracted spectrum using IRAF routines with flux standard spectra taken each night. Where possible, all extracted spectra were then assigned a spectral classification

²http://www.ociw.edu/lco/magellan/instruments/LDSS2/ldss2_usersguide.html

by visual inspection and comparison with published atlases of optical and near-IR spectra (62; 33; 9; 2).

3. Analysis

3.1. Extinction and Hydrogen Column Density

To estimate the hydrogen column density N_H for all X-ray-optical matches observed with LDSS2, we use the flux-calibrated *optical* spectrum of each candidate optical counterpart. We fit the spectrum with a blackbody attenuated by interstellar reddening, using the analytical parameterization of the average Galactic extinction law $E(\lambda-V)/E(B-V)$ given by Howarth (31). We limit the region to be fitted to the central part of the spectra: 5500–6700Å; in part to simplify the fitting procedure, and also because the flux calibrated spectra anomalously fall off in flux redward of $\sim 7000\text{Å}$. We also interpolate over major spectral lines at 5575, 6300 and 6562Å and in the case of the molecular bands present in M type stars we fit a smooth continuum shape to the star at 3–4 points between bands (we use a Legendre polynomial of order 10) and fit to this instead. Using a fixed effective temperature (T_{eff}), estimated from our spectral type determination from spectral lines, we fit for $E(B-V)$ and a normalization factor: R^2/d^2 (radius of object R , distance d). We obtain A_V from the standard relation $A_V = 3.1 \times E(B-V)$ and the hydrogen column density from $N_H = 1.79 \times 10^{21} \times A_V \text{ cm}^{-2}$ (from 45). The T_{eff} in each case is representative of the spectral type range we were able to estimate given only visual classification of each spectrum and no constraint on luminosity class (i.e. A/F means A8 to F2, luminosity class undetermined). The fit is independent of any X-ray emission properties. Effective temperatures and adopted photometry for each spectral type ‘bin’ are given in Table 4 below, (see references listed in the table). Example fits for a K and an M (polynomial fit) star are shown in Figure 1.

To test the above, we derive comparison N_H values using our V , R and I photometry (where available). We calculate $E(V-R) \equiv V-R-(V-R)_0$ and $E(R-I) \equiv R-I-(R-I)_0$, selecting appropriate values for the intrinsic $(V-R)_0$ and $(R-I)_0$ colors (from 10) for a given spectral type (see Table 4). From Dopita & Sutherland (15) we find: $A_V = 3.97 \times E(V-R)$ and $A_V = 3.76 \times E(R-I)$ and we convert to N_H as above. Figure 2 below shows spectral fit-determined values of N_H against the color determined results. The values are correlated somewhat, but the spectral fit N_H is systematically higher than that from photometry: from a simple linear regression test we find $N_H(fit) = 0.96 \pm 0.09(N_H(R-I)) + 0.2$ and $N_H(fit) = 0.81 \pm 0.07(N_H(V-R)) + 0.25$. Dropping the five highest points in either plot however, worsens the correlation: $N_H(fit) = 0.81 \pm 0.13(N_H(R-I)) + 0.27$ and $N_H(fit) = 0.65 \pm 0.1(N_H(V-R)) + 0.3$. This overestimate in N_H is also seen in a

Table 3. X-ray to Optical Matching Summary

| Field Name | N(X) ^a | N(Xmatch) ^b | N(Opt) ^c | N(Spectra) ^d | N(Id. Spec.) ^e |
|------------|-------------------|------------------------|---------------------|-------------------------|---------------------------|
| J1655 | 137 | 58 | 227 | 32 | 28 |
| G347b | 108 | 53 | 147 | 26 | 25 |
| SgrB2 | 369 | 112 | 165 | 52 | 45 |
| GalCA | 222 | 48 | 67 | 9 | 9 |
| SgrA★ | 2982 | 327 | 340 | 17 | 15 |
| Total | 3818 | 598 | 946 | 136 | 122 |

Note. — ^aThe number of unique (level 1) X-ray sources in all bands. ^bThe number of X-ray sources that have any optical counterpart(s). ^cThe number of optical sources falling inside 2σ error circles. Some X-ray sources match multiple optical sources. ^dThe number of optical spectra of *Chandra* matches obtained with LDSS2. ^eThe number of *identifiable* spectra from this sample.

Table 2. Spectral Observations with LDSS2/Magellan 6.5m

| Date | Fields Observed | Flux Standards Used | Grism/Filter ^a |
|-----------------|----------------------------------|----------------------------|---------------------------|
| May 18–20 2001 | SgrA | LTT3864, LTT7987 | MedRed/S2 |
| July 25–27 2001 | SgrB2 | LTT9239, Feige110, LTT7379 | MedBlue/None |
| June 16–19 2002 | J1655, GalCA, SgrA, SgrB2, G347b | LTT9239, EG274 | MedBlue/None |

^a2nd order blocking filter

color-magnitude diagram for our stellar sources (Figure 3) of absolute visual magnitude M_V against dereddened color $V - R$. A comparison main sequence is plotted using the data from Table 4. We estimate the systematic excess in A_V from our fitting technique to be 1.1 (equivalent to N_H of $2 \times 10^{21} \text{cm}^{-2}$). This overestimate is perhaps due to the inadequacy of the black-body spectrum as a fit to late-type stellar spectra over this wavelength range where many absorption lines significantly modify the continuum shape.

Table 4. Effective Temperature Assignment and Photometric Properties Used

| Classification | Sp. Type Range | T_{eff} (K) | V–R | R–I | M_V |
|----------------|----------------|---------------|------|------|----------------|
| Early A | A2–A4 | 9100 | 0.08 | 0.03 | 1.8 ± 0.4 |
| Mid A | A4–A6 | 8500 | 0.16 | 0.06 | 2.0 ± 0.5 |
| Late A | A6–A8 | 7700 | 0.19 | 0.09 | 2.4 ± 0.6 |
| A/F | A8–F2 | 7200 | 0.30 | 0.17 | 2.8 ± 0.6 |
| Early F | F2–F4 | 6750 | 0.35 | 0.20 | 3.2 ± 0.4 |
| Mid F | F4–F6 | 6500 | 0.40 | 0.24 | 3.5 ± 0.4 |
| Late F | F6–F8 | 6200 | 0.47 | 0.29 | 3.8 ± 0.4 |
| F/G | F8–G2 | 5950 | 0.50 | 0.31 | 4.3 ± 0.7 |
| Early G | G2–G4 | 5600 | 0.53 | 0.33 | 4.6 ± 0.4 |
| Mid G | G4–G6 | 5400 | 0.60 | 0.42 | 4.9 ± 0.5 |
| Late G | G6–G8 | 5200 | 0.64 | 0.43 | 5.3 ± 0.5 |
| G/K | G8–K2 | 5050 | 0.70 | 0.48 | 5.8 ± 1.0 |
| Early K | K2–K4 | 4700 | 0.80 | 0.53 | 6.7 ± 0.6 |
| Mid K | K4–K6 | 4300 | 1.10 | 0.75 | 7.4 ± 0.6 |
| Late K | K6–K8 | 4000 | 1.15 | 0.78 | 8.4 ± 0.6 |
| K/M | K8–M2 | 3700 | 1.25 | 0.93 | 9.3 ± 1.0 |
| Early M | M2–M4 | 3400 | 1.42 | 1.15 | 11.1 ± 1.6 |
| Mid M | M4–M6 | 3000 | 1.8 | 1.67 | 13.2 ± 2.0 |

Note. — References for colors, temperatures and absolute magnitudes: Johnson (34), Bessell (6), Mikami & Heck (39), Houk et al. (30), Gray (23), Cox (10). We estimate an uncertainty in the assigned T_{eff} values of $\pm 500\text{K}$, based on the spread of values found in the various references.

Table 5. Combined Results for 2σ Optical Matches

| ChOPS ID ^a (1) | Type ^b (2) | Special ^c (3) | Counts ^d (4) | N_{22} ^e (5) | $\log(F_x/F_R)$ ^f (6) | Dist. ^g (7) | M_V (8) | $\log(L_x)$ ^h (9) | R (10) | N_M ⁱ (11) | Srch ^j (12) | Offset ^j (13) | P_{RR} ^j (14) |
|------------------------------|--------------------------|-----------------------------|----------------------------|------------------------------|-------------------------------------|---------------------------|--------------|---------------------------------|-----------|----------------------------|---------------------------|-----------------------------|-------------------------------|
| J1655 | | | | | | | | | | | | | |
| J165343.19–394826.1 | G/K | ... | 11±5 | 0.3(1) | -2.5±0.4 | 1.4 | 5.7(9) | 29.54±0.7 | 17.48(1) | 1 | 1.199 | 0.420 | 0.207 |
| J165350.37–394621.9 | midM dMe? | ... | 12±5 | 0.2(2) | -1.8±0.5 | 1.4 | 8(2) | 29.43±0.8 | 19.32(1) | 2 | 1.886 | 1.271 | 0.712 |
| J165350.70–395339.6 | earlyK | ... | 8±5 | 0.3(1) | -2.2±0.4 | 1.5 | 6.8(9) | 29.46±0.7 | 18.44(1) | 1 | 0.858 | 0.788 | 0.082 |
| J165351.90–394812.7 | F/G? | <i>by</i> | 18±6 | 0.7(2) | -1.8±0.6 | 4.0 | 5(2) | 30.59±0.8 | 20.63(1) | 1 | 0.715 | 0.692 | 0.064 |
| J165354.54–394741.0 | G? | <i>rs</i> | 11±5 | 0.9(2) | -3.5±0.7 | 4.5 | 1(1) | 30.38±5.9 | 17.96(1) | 1 | 0.874 | 0.322 | 0.092 |
| J165356.10–394732.7 | lateF | ... | 9*±5 | 0.4(2) | -3.1±0.5 | 1.9 | ... | 29.87±0.7 | 16.30(1) | 1 | 0.933 | 0.391 | 0.113 |
| J165356.98–394636.7 | earlyG | ... | 8*±5 | 0.9(2) | -2.8±0.6 | 4.8 | 2(2) | 30.81±5.4 | 19.10(3) | 1 | 1.322 | 0.358 | 0.271 |
| J165357.34–394847.9 | midM dMe? | ... | 18±5 | 0.2(1) | -1.3±0.4 | 1.1 | 9.9(9) | 29.43±0.7 | 19.93(2) | 1 | 0.677 | 0.380 | 0.050 |
| J165357.85–395032.1 | F/G? | ... | 6*±4 | 0.6(1) | -2.5±0.5 | 3.1 | 4.1(9) | 30.12±0.8 | 19.20(1) | 1 | 0.584 | 0.230 | 0.024 |
| J165358.28–394812.6 | midM | ... | 6*±4 | 0.1(1) | -2.1±0.5 | 0.8 | 10.0(8) | 28.50±0.8 | 19.25(1) | 1 | 1.045 | 0.510 | 0.163 |
| J165358.44–394745.6 | early/midM | ... | 15±5 | 0.2(2) | -2.4±0.6 | 1.2 | 7(2) | 29.46±0.7 | 17.45(1) | 1 | 0.842 | 0.211 | 0.081 |
| J165359.83–394856.1 | early/midM dMe | ... | 9±4 | 0.3(3) | -1.8±0.6 | 1.4 | ... | 29.40±0.8 | 19.58(2) | 1 | 0.698 | 0.399 | 0.052 |
| J165400.14–395045.1 | F3–6IV | <i>q</i> | 64±9 | 0.6(1) | -2.9±0.4 | 2.8 | 1.2(9) | 30.86±0.7 | 16.14(1) | 1 | 0.412 | 0.218 | 0.015 |
| J165400.81–395145.5 | earlyM dMe? | ... | 24±6 | 0.4(1) | -0.9±0.4 | 2.0 | ... | 30.04±0.7 | 21.50(5) | 1 | 0.444 | 0.237 | 0.013 |
| J165402.81–395104.8 | earlyG | ... | 8*±4 | 0.4(2) | -2.7±0.5 | 2.2 | 4(2) | 29.88±0.8 | 17.77(1) | 1 | 0.511 | 0.268 | 0.017 |
| J165403.00–394816.3 | midM dMe | ... | 17±5 | 0.2(1) | -1.2±0.4 | 1.1 | 10.6(9) | 29.26±0.7 | 20.56(1) | 1 | 0.711 | 0.360 | 0.055 |
| J165403.27–395217.2 | midlateG | ... | 14±5 | 0.4(4) | -2.5±0.8 | 2.1 | 4(3) | 30.08±0.8 | 17.58(1) | 1 | 0.484 | 0.275 | 0.017 |
| J165403.64–395054.7 | lateG | ... | 23±6 | 0.3(1) | -2.2±0.4 | 1.6 | 5.6(9) | 29.90±0.7 | 17.77(1) | 1 | 0.456 | 0.197 | 0.015 |
| J165404.79–394817.4 | G/K(| <i>rs</i> | 21±6 | 0.8(2) | -2.7±0.5 | 4.0 | 1(1) | 31.05±1.2 | 17.64(1) | 1 | 0.636 | 0.451 | 0.046 |
| J165404.89–394934.5 | K/M | ... | 9±4 | 0.2(1) | -2.2±0.4 | 0.9 | 8.1(9) | 28.99±0.7 | 18.19(2) | 1 | 0.625 | 0.474 | 0.036 |
| J165407.44–394542.7 | ? | ... | 13±6 | <3.5 | > -1.3 | <2.4 | >7.43 | <30.2 | 20.87(1) | 3 | 2.172 | 1.383 | 0.950 |
| J165408.14–395636.1 | midG | <i>q</i> | 86±10 | 0.4(1) | -2.7±0.5 | 2.2 | 3(1) | 31.00±0.7 | 16.19(2) | 1 | 0.724 | 0.170 | 0.056 |
| J165411.04–395200.6 | midM? dMe | ... | 9±4 | 0.5(1) | -1.3±0.4 | 2.3 | 8.0(9) | 30.03±0.7 | 21.14(2) | 1 | 0.635 | 0.105 | 0.029 |
| J165411.38–395236.8 | early/midG | <i>rs</i> | 13±5 | 0.8(2) | -2.8±0.5 | 3.9 | ... | 31.00±1.1 | 17.51(1) | 1 | 0.601 | 0.380 | 0.032 |
| J165412.28–395434.2 | mid/lateG | ... | 41±8 | 0.3(2) | -2.6±0.5 | 1.7 | 3(2) | 30.43±0.7 | 15.75(1) | 1 | 0.668 | 0.232 | 0.042 |
| J165413.21–395005.1 | early/midK | ... | 6*±4 | 0.2(1) | -2.8±0.4 | 1.3 | 6.1(9) | 29.18±0.7 | 17.25(1) | 1 | 0.814 | 0.169 | 0.072 |
| J165413.51–394757.0 | mid/lateF | ... | 7*±4 | 0.2(1) | -3.4±0.4 | 1.3 | ... | 29.15±0.7 | 15.92(1) | 1 | 1.152 | 0.210 | 0.183 |
| J165413.47–395757.6 | ? | ... | 22±6 | <0.5† | > -1.0 | <2.5 | >7.86 | <30.5 | 21.33(3) | 1 | 1.647 | 1.257 | 0.406 |
| J165419.80–395445.8 | ? | ... | 11±5 | <0.01† | > -1.7 | <0.1 | >15.7 | <27.0 | 19.62(1) | 1 | 1.673 | 0.650 | 0.511 |
| J165422.01–395205.0 | midM dMe | ... | 12±5 | 0.2(2) | -1.5±0.5 | 1.3 | 9(2) | 29.58±0.7 | 19.57(1) | 1 | 0.972 | 0.920 | 0.087 |
| J165424.36–395141.0 | early/midK | ... | 10±5 | 0.04(14) | -3.2±0.4 | 0.2 | ... | 27.85±0.8 | 15.32(1) | 1 | 1.519 | 0.217 | 0.317 |
| J165427.11–395231.4 | ? | ... | 21±6 | <1.0 | > -1.9 | <6.3 | >1.71 | <31.7 | 20.01(1) | 1 | 1.500 | 0.208 | 0.324 |
| G347b | | | | | | | | | | | | | |
| J171447.10–395247.1 | lateG | ... | 25±8 | 0.6(1) | -2.6±0.5 | 2.4 | 4.0(9) | 30.32±0.7 | 18.22(2) | 1 | 2.190 | 0.790 | 0.514 |
| J171448.72–395617.3 | G? | <i>rs</i> | 9*±5 | 1.3(2) | -2.7±0.6 | 4.2 | 2(1) | 30.98±0.7 | 20.20(1) | 1 | 2.043 | 1.002 | 0.456 |
| J171452.55–395640.0 | lateG | ... | 22±6 | 0.6(1) | -2.4±0.4 | 2.3 | 3.8(9) | 30.53±0.6 | 17.95(1) | 1 | 0.961 | 0.173 | 0.104 |
| J171503.40–395416.2 | lateF | ... | 11±5 | 0.6(1) | -2.2±0.5 | 2.0 | 5.7(9) | 29.96±0.7 | 19.25(2) | 1 | 1.011 | 0.475 | 0.116 |
| J171507.76–395407.5 | ? | ... | 8*±4 | >10.0 | ... | ... | ... | ... | 21.85(3) | 1 | 1.170 | 0.650 | 0.168 |
| J171508.43–395530.9 | earlyK | <i>rs</i> | 10±5 | 1.1(1) | ... | 3.7 | 4(1) | 30.94±0.6 | 21.03(5) | 1 | 0.756 | 0.256 | 0.069 |
| J171509.91–395429.6 | lateF? | ... | 8*±4 | 0.9(1) | -2.2±0.5 | 3.4 | 4(1) | 30.63±0.6 | 19.82(1) | 1 | 1.128 | 0.555 | 0.158 |
| J171510.54–395603.5 | earlyA | ... | 13±5 | 0.5(2) | -3.4±0.6 | 2.1 | ... | 30.34±0.6 | 14.96(1) | 1 | 0.655 | 0.639 | 0.049 |
| J171513.56–395456.6 | G/K? | <i>tt</i> | 12±5 | 0.6(1) | -2.5±0.4 | 2.7 | 3.4(9) | 30.61±0.6 | 18.00(1) | 1 | 0.760 | 0.425 | 0.068 |
| J171513.65–400112.3 | mid/lateG | ... | 20±6 | 0.5(2) | -2.1±0.5 | 2.1 | ... | 30.55±0.6 | 17.81(1) | 1 | 0.653 | 0.371 | 0.048 |
| J171513.90–395743.4 | earlyG | ... | 10±5 | 0.6(1) | -2.6±0.5 | 2.7 | 4.0(9) | 30.22±0.6 | 18.32(1) | 1 | 0.517 | 0.299 | 0.027 |
| J171516.16–395844.1 | midG | ... | 8*±4 | 0.7(2) | -3.1±0.6 | 3.0 | 2(2) | 30.58±0.6 | 16.952(4) | 1 | 0.571 | 0.474 | 0.026 |
| J171517.18–395535.7 | F/G? | ... | 9±4 | 0.8(1) | -2.3±0.6 | 3.0 | 4(1) | 30.36±0.7 | 19.73(1) | 1 | 0.692 | 0.337 | 0.059 |
| J171518.23–400147.9 | K/M dMe | ... | 12±5 | 0.5(1) | -1.4±0.4 | 2.2 | 8(1) | 30.19±0.6 | 20.46(1) | 1 | 1.386 | 1.020 | 0.224 |
| J171519.78–400411.6 | G/K? | ... | 12*±6 | 0.8(2) | -2.5±0.5 | 3.0 | 3(1) | 30.81±0.6 | 17.995(4) | 1 | 1.630 | 1.219 | 0.271 |

Table 5—Continued

| ChOPS ID ^a (1) | Type ^b (2) | Special ^c (3) | Counts ^d (4) | N_{22} ^e (5) | $\log(F_x/F_R)$ ^f (6) | Dist. ^g (7) | M_V (8) | $\log(L_x)$ ^h (9) | R (10) | N_M ⁱ (11) | Srch ^j (12) | Offset ^j (13) | P_{Rn} ^j (14) |
|------------------------------|--------------------------|-----------------------------|----------------------------|------------------------------|-------------------------------------|---------------------------|--------------|---------------------------------|-----------|----------------------------|---------------------------|-----------------------------|-------------------------------|
| J171520.17–400248.2 | G? | <i>by</i> | 56±9 | 0.6(2) | ... | 2.5 | 6(1) | 31.04±0.5 | 20.05(3) | 1 | 0.691 | 0.343 | 0.054 |
| J171520.66–395934.9 | F/G | ... | 5*±4 | 0.5(1) | -3.1±0.5 | 2.2 | 3(1) | 30.05±0.6 | 16.86(1) | 2 | 0.793 | 0.354 | 0.077 |
| J171523.89–400026.8 | lateK | <i>rs</i> | 13±5 | 0.7(2) | -2.6±0.5 | 2.9 | 3(2) | 30.82±0.6 | 16.80(1) | 1 | 0.577 | 0.556 | 0.040 |
| J171524.21–395950.9 | lateG | <i>rs</i> | 17±5 | 0.7(2) | -2.8±0.5 | 2.8 | 1(1) | 30.98±0.6 | 16.83(1) | 1 | 0.644 | 0.364 | 0.048 |
| J171525.99–395603.9 | lateG? | ... | 18±6 | 1.0(6) | -3.0±1.2 | 3.6 | 1(5) | 31.03±0.7 | 17.93(1) | 1 | 0.609 | 0.535 | 0.042 |
| J171528.22–395929.4 | midG | ... | 9±5 | 0.6(1) | -2.2±0.5 | 2.7 | 4.7(9) | 30.33±0.6 | 19.23(1) | 1 | 0.768 | 0.437 | 0.063 |
| J171529.77–400309.2 | lateA | ... | 14±6 | 0.4(2) | -3.1±0.5 | 1.8 | 3(2) | 30.00±0.6 | 16.06(2) | 1 | 2.004 | 1.086 | 0.404 |
| J171531.96–395259.3 | midG | <i>by</i> | 18±6 | 0.7(1) | -1.1±0.4 | 3.0 | 7(1) | 30.94±0.6 | 21.18(3) | 1 | 1.343 | 0.678 | 0.189 |
| J171532.99–400220.4 | midM | ... | 19±7 | 0.2(2) | -2.1±0.5 | 1.1 | 7(2) | 29.71±0.6 | 17.317(4) | 1 | 1.100 | 0.770 | 0.114 |
| J171536.42–395532.7 | earlyG | ... | 11±5 | 0.5(1) | -2.7±0.4 | 2.1 | 3.6(9) | 30.25±0.6 | 17.08(1) | 1 | 1.079 | 0.288 | 0.099 |
| J171537.99–395739.2 | early/midG | ... | 14±5 | 0.6(1) | -2.1±0.4 | 2.5 | 4.9(9) | 30.44±0.6 | 18.74(1) | 1 | 0.934 | 0.418 | 0.063 |
| SgrB2 | | | | | | | | | | | | | |
| J174633.29–282512.7 | mid/lateF | ... | 25±9 | 0.8(2) | -3.3±0.5 | 1.3 | 3(1) | 30.07±1.3 | 16.52(1) | 2 | 2.017 | 1.464 | 0.282 |
| J174634.65–282721.1 | ? | ... | 33±8 | >2.0 | < -3.2 | >2.3 | < -0.09 | >30.7 | 21.18(2) | 3 | 3.641 | 3.440 | 1.749 |
| J174639.48–282804.3 | G/K | ... | 24±7 | 0.6(2) | -2.7±0.5 | 1.0 | 5(2) | 29.64±1.5 | 17.667(4) | 1 | 1.146 | 0.097 | 0.086 |
| J174640.67–282417.1 | F/G | ... | 25±7 | 0.4(2) | -3.7±0.5 | 0.7 | 4(2) | 29.24±1.6 | 14.53(1) | 1 | 1.213 | 1.153 | 0.100 |
| J174642.22–282907.4 | K | ... | 21±7 | 2.5(4) | -5.2±0.9 | 2.6 | -4(3) | 30.88±1.2 | 18.08(1) | 1 | 1.171 | 0.885 | 0.072 |
| J174645.48–282926.2 | F/G | ... | 225±16 | 0.5(2) | -3.3±0.5 | 0.9 | 1(1) | 30.47±1.5 | 13.54(2) | 1 | 0.561 | 0.419 | 0.018 |
| J174647.09–282426.1 | mid/lateG | ... | 12*±6 | 0.6(2) | -4.1±1.9 | 0.9 | 6(1) | 28.10±2.4 | 17.506(2) | 1 | 1.108 | 0.696 | 0.087 |
| J174649.08–282645.6 | G/K | ... | 11±5 | 0.7(3) | -2.7±0.6 | 1.0 | 6(2) | 29.37±1.5 | 18.52(1) | 1 | 1.015 | 0.749 | 0.063 |
| J174649.59–282338.1 | midM dMe | ... | 13±6 | 0.3(3) | -2.1±0.6 | 0.5 | 10(2) | 28.53±1.7 | 18.82(1) | 1 | 2.399 | 0.899 | 0.917 |
| J174650.65–282839.8 | lateF | ... | 32±7 | 0.6(2) | -3.3±0.5 | 1.0 | 3(1) | 29.74±1.5 | 15.75(9) | 1 | 0.687 | 0.110 | 0.033 |
| J174651.71–283030.2 | midM dMe | ... | 40±8 | 0.1(2) | -1.9±0.5 | 0.2 | 12(2) | 28.17±2.2 | 18.04(2) | 1 | 0.787 | 0.410 | 0.051 |
| J174652.63–282503.1 | F/G? | ... | 33±7 | 0.6(2) | -2.8±0.5 | 0.9 | 5(1) | 29.69±1.5 | 16.709(4) | 1 | 0.647 | 0.550 | 0.031 |
| J174653.22–282830.9 | lateG | <i>rs</i> | 209±16 | 0.6(2) | -3.2±0.5 | 1.0 | 1(2) | 30.64±1.4 | 13.99(2) | 1 | 0.458 | 0.201 | 0.014 |
| J174656.41–282811.2 | earlyK | ... | 17±6 | 0.6(2) | -2.5±0.6 | 1.0 | 7(2) | 29.34±1.5 | 18.749(4) | 1 | 0.628 | 0.233 | 0.026 |
| J174658.35–282617.3 | lateG? | ... | 13±5 | 0.6(2) | -4.4±0.5 | 0.9 | 2(2) | 29.25±1.5 | 13.70(7) | 1 | 0.582 | 0.389 | 0.017 |
| J174659.34–282139.1 | F/G? | ... | 27±7 | 0.8(2) | -2.2±0.5 | 1.2 | 6(1) | 29.84±1.4 | 19.35(1) | 1 | 0.972 | 0.295 | 0.068 |
| J174700.24–282236.0 | earlyM dMe? | ... | 14±5 | 0.5(2) | -1.8±0.6 | 0.9 | 9(2) | 29.30±1.5 | 20.05(1) | 1 | 0.906 | 0.237 | 0.062 |
| J174700.72–283204.9 | midM dMe | ... | 444±22 | 0.2(2) | -1.4±0.4 | 0.3 | 10(1) | 29.61±1.9 | 16.86(1) | 1 | 0.518 | 0.390 | 0.020 |
| J174706.77–283356.4 | midM | ... | 17*±8 | 0.1(1) | -2.7±0.4 | 0.3 | 10(1) | 27.94±2.1 | 17.02(3) | 1 | 2.231 | 1.546 | 0.438 |
| J174708.21–282724.8 | G? | ... | 7*±4 | 0.8(2) | -2.5±0.5 | 1.2 | 6(1) | 29.42±1.4 | 19.78(1) | 1 | 0.564 | 0.423 | 0.017 |
| J174709.30–282317.5 | F/G | ... | 10±5 | 0.8(1) | -2.9±0.5 | 1.2 | 5(1) | 29.68±1.4 | 18.13(1) | 1 | 0.905 | 0.199 | 0.088 |
| J174710.66–282828.4 | early/midG | ... | 29±7 | 0.5(2) | -2.6±0.5 | 0.8 | 6(2) | 29.39±1.5 | 17.18(1) | 1 | 0.483 | 0.197 | 0.026 |
| J174711.42–282533.9 | F/G? | ... | 8*±4 | 1.0(1) | -3.1±0.6 | 1.4 | 5(1) | 29.26±1.4 | 19.86(1) | 1 | 0.575 | 0.219 | 0.023 |
| J174712.39–282836.9 | G? | ... | 23±6 | 0.9(2) | -2.5±0.5 | 1.3 | 5(2) | 30.00±1.3 | 18.94(1) | 1 | 0.538 | 0.287 | 0.022 |
| J174713.11–282906.4 | K/M | ... | 7±4 | 0.4(1) | -2.1±0.4 | 0.7 | 9(1) | 28.81±1.6 | 19.46(1) | 1 | 0.733 | 0.132 | 0.035 |
| J174713.29–282037.4 | G/K | ... | 53±9 | 0.8(2) | -2.2±0.5 | 1.2 | 5(1) | 30.26±1.3 | 18.37(1) | 1 | 0.812 | 0.115 | 0.026 |
| J174714.12–282528.3 | midK | ... | 19±6 | 0.1(2) | -2.2±0.4 | 0.3 | 11(1) | 28.01±2.1 | 17.91(1) | 1 | 0.504 | 0.250 | 0.012 |
| J174714.27–282108.4 | K/M dMe | ... | 31±8 | 0.4(2) | -2.1±0.5 | 0.6 | 8(2) | 29.11±1.6 | 18.12(1) | 1 | 0.977 | 0.101 | 0.075 |
| J174714.77–282811.4 | ? | ... | 34±7 | 0.9(2) | -7.2±2.8 | 1.3 | -12(12) | 30.87±1.3 | 17.79(2) | 1 | 0.485 | 0.115 | 0.016 |
| J174715.50–283155.7 | earlyM dMe | ... | 18±7 | 0.4(3) | -2.2±0.6 | 0.6 | 9(2) | 28.89±1.6 | 18.49(1) | 1 | 1.137 | 0.583 | 0.185 |
| J174715.82–282643.1 | G/K | ... | 11±5 | 0.6(1) | -2.7±0.4 | 1.0 | 6.1(9) | 29.27±1.5 | 18.49(1) | 1 | 0.570 | 0.316 | 0.036 |
| J174717.98–282729.3 | midM dMe | ... | 13±5 | 0.5(3) | -1.8±0.6 | 0.8 | 10(2) | 28.97±1.6 | 20.13(2) | 1 | 0.666 | 0.233 | 0.026 |
| J174718.27–282753.3 | earlyG | ... | 16±6 | 0.4(1) | ... | 0.7 | 10(1) | ... | 19.82(2) | 1 | 0.622 | 0.611 | 0.023 |
| J174719.59–282204.9 | lateG? | ... | 4*±5 | 0.9(2) | ... | 1.3 | 6(1) | ... | 20.05(1) | 3 | 4.128 | 3.930 | 1.874 |
| J174720.10–282437.8 | ? | ... | 10±5 | 2.4(2) | -7.0±6.1 | 2.5 | ... | 31.60±1.8 | 20.08(3) | 1 | 0.941 | 0.437 | 0.077 |
| J174720.16–282823.6 | midM dMe | ... | 11±5 | 0.1(1) | -1.3±0.4 | 0.3 | 15.0(8) | 27.70±2.1 | 20.99(2) | 1 | 0.867 | 0.207 | 0.068 |
| J174721.24–281928.5 | ? | ... | 24±8 | >10.0† | ... | >6.0 | ... | ... | 20.75(2) | 1 | 2.477 | 1.219 | 0.388 |
| J174722.25–282530.0 | lateF | ... | 12±5 | 0.2(2) | -4.1±0.5 | 0.4 | 6(2) | 28.05±1.9 | 14.21(1) | 1 | 0.821 | 0.141 | 0.052 |

Table 5—Continued

| ChOPS ID ^a (1) | Type ^b (2) | Special ^c (3) | Counts ^d (4) | N_{22} ^e (5) | $\log(F_x/F_R)$ ^f (6) | Dist. ^g (7) | M_V (8) | $\log(L_x)$ ^h (9) | R (10) | N_M ⁱ (11) | Srch ^j (12) | Offset ^j (13) | P_{Rn} ^j (14) |
|------------------------------|--------------------------|-----------------------------|----------------------------|------------------------------|-------------------------------------|---------------------------|--------------|---------------------------------|-----------|----------------------------|---------------------------|-----------------------------|-------------------------------|
| J174723.15–282747.6 | ? | ... | 12±5 | <3.0† | > -5.1 | <3.0 | ... | <30.0 | 22.78(6) | 1 | 1.662 | 0.841 | 0.937 |
| J174723.36–282534.0 | ? | ... | 62±9 | 2.3(2) | ... | 2.5 | ... | ... | 20.42(2) | 1 | 0.533 | 0.393 | 0.023 |
| J174725.59–282930.8 | lateA | ... | 7*±5 | 0.6(2) | -3.7±0.5 | 1.1 | 4(1) | 29.16±1.4 | 16.32(1) | 1 | 1.436 | 0.318 | 0.238 |
| J174726.89–283309.1 | midG | ... | 27±9 | 0.2(1) | -2.8±0.4 | 0.3 | 10.0(9) | 27.87±2.0 | 17.28(2) | 1 | 2.506 | 1.621 | 0.464 |
| J174727.64–282646.5 | early/midG | ... | 34±7 | 0.5(2) | -2.7±0.4 | 0.8 | 6(1) | 29.46±1.5 | 17.05(1) | 1 | 0.680 | 0.253 | 0.025 |
| J174731.11–282513.0 | mid/lateF | ... | 18±7 | 0.5(2) | -2.9±0.5 | 0.9 | 7(1) | 28.93±1.5 | 18.15(1) | 1 | 3.011 | 0.390 | 1.673 |
| J174732.09–282033.8 | G/K? | tt | 53±10 | 0.5(2) | -2.7±0.5 | 0.8 | 6(2) | 29.71±1.5 | 16.15(1) | 1 | 1.559 | 0.884 | 0.149 |
| J174733.60–281840.6 | lateF? | ... | 48±11 | 0.4(1) | -4.0±0.4 | 0.8 | 2(1) | 29.65±1.5 | 12.98(1) | 1 | 1.994 | 1.531 | 0.123 |
| J174734.60–283216.6 | K/M dMe | ... | 95±12 | 0.3(1) | -2.2±0.3 | 0.5 | 7.7(9) | 29.35±1.7 | 16.28(1) | 1 | 1.045 | 0.409 | 0.032 |
| J174735.64–282011.4 | lateG | ... | 120±14 | 0.6(2) | -2.7±0.5 | 1.0 | 4(1) | 30.25±1.5 | 15.95(1) | 1 | 1.091 | 0.587 | 0.104 |
| J174736.39–283214.0 | F/G | ... | 116±14 | 0.3(1) | -2.4±0.3 | 0.4 | 6.9(9) | 29.37±1.7 | 15.55(1) | 1 | 1.015 | 0.799 | 0.050 |
| J174737.58–282228.7 | midK | ... | 20±8 | 0.2(2) | -2.3±0.5 | 0.3 | 10(2) | 28.28±2.0 | 17.57(1) | 1 | 1.699 | 0.575 | 0.183 |
| J174737.90–282040.6 | ? | ... | 43±11 | <2.0† | >2.5 | <2.3 | >0.86 | <31.0 | 21.59(2) | 1 | 1.689 | 1.170 | 0.174 |
| J174746.14–282350.5 | earlyG | ... | 20*±10 | 0.8(1) | ... | 1.2 | 5(1) | ... | 18.44(1) | 1 | 2.483 | 1.400 | 0.826 |
| GalCA | | | | | | | | | | | | | |
| J174614.20–285136.4 | lateG | ... | 127±13 | 0.7(1) | -2.0±0.3 | 1.1 | 4.4(9) | 30.70±1.4 | 16.97(1) | 1 | 0.407 | 0.258 | 0.010 |
| J174611.12–284933.9 | G? | ... | 10*±5 | 0.5(2) | -2.2±0.5 | 0.8 | 7(2) | 29.40±1.5 | 18.45(1) | 1 | 1.161 | 0.707 | 0.081 |
| J174618.87–285145.9 | late/midF | ... | 12±5 | 0.1(1) | -3.6±0.4 | 0.2 | 8(1) | 27.62±2.3 | 14.10(1) | 1 | 0.489 | 0.137 | 0.015 |
| J174626.49–285411.1 | early/midA | ... | 3*±4 | 0.3(2) | -3.8±0.5 | 1.1 | 4(1) | 29.09±0.9 | 15.04(1) | 1 | 0.685 | 0.027 | 0.032 |
| J174629.36–285100.8 | G?(by) | by | 12±5 | 0.5(2) | -1.6±0.5 | 0.8 | 9(2) | 29.54±1.5 | 19.57(1) | 1 | 0.594 | 0.097 | 0.024 |
| J174630.19–285442.1 | midM | ... | 23±6 | 0.2(1) | -1.6±0.4 | 0.3 | 12.2(9) | 28.41±2.0 | 18.82(1) | 1 | 0.636 | 0.096 | 0.026 |
| J174637.44–285108.7 | midM dMe | ... | 13±5 | 0.00(1) | -1.6±0.3 | 0.1 | 16.6(5) | 26.71±0.2 | 18.61(1) | 1 | 0.895 | 0.416 | 0.057 |
| J174638.02–285326.2 | CV-A | cv | 438±22 | 1.4(3)† | 1.2±0.6 | 1.8 | 3(2) | 31.87±1.2 | 20.23(2) | 1 | 0.447 | 0.317 | 0.013 |
| J174656.89–285233.9 | CV-C | cv | 30±12 | >1.4† | < -2.3 | >1.7 | <3.99 | >30.2 | 21.30(2) | 1 | 2.36 | 2.03 | 0.401 |
| SgrA | | | | | | | | | | | | | |
| J174511.51–290236.8 | K/M dMe | ... | 83±18 | 0.8(5) | -2.5±0.9 | 2.3 | 5(4) | 30.21±0.7 | 19.23(1) | 1 | 0.899 | 0.868 | 0.045 |
| J174516.18–290315.8 | ? | ... | 728±32 | 6(1) | -7.6±2.1 | 11.5 | ... | 33.64±0.7 | 22.31(5) | 1 | 0.497 | 0.221 | 0.015 |
| J174517.75–290139.3 | lateG? | ... | 212±19 | 0.2(3) | -2.4±0.6 | 1.3 | 6(2) | 29.75±0.6 | 17.04(1) | 1 | 0.525 | 0.111 | 0.016 |
| J174520.62–290152.1 | midM dMe | ... | 1071±35 | 0.3(3) | -1.3±0.6 | 1.4 | 7(2) | 30.47±0.7 | 18.22(1) | 1 | 0.429 | 0.209 | 0.011 |
| J174522.76–290018.5 | ? | ... | 107±14 | <0.001† | > -2.3 | <0.1 | >13.7 | <26.9 | 17.83(1) | 1 | 0.505 | 0.151 | 0.013 |
| J174528.08–285726.5 | midM dMe | ... | 136±16 | 0.00(6) | -2.0±0.3 | 0.1 | 15.8(7) | 26.52±0.0 | 17.97(1) | 1 | 0.475 | 0.034 | 0.011 |
| J174530.63–290441.0 | F/G | ... | 127±16 | 0.4(3) | -2.7±0.6 | 1.4 | 5(2) | 29.69±0.7 | 17.17(1) | 1 | 0.556 | 0.234 | 0.019 |
| J174537.99–290134.5 | A/F? | ... | 290±22 | 3(1) | -5.2±1.7 | 4.5 | -7(7) | 32.08±0.8 | 18.45(1) | 1 | 0.383 | 0.105 | 0.009 |
| J174538.28–285602.7 | midM dMe | ... | 202±18 | 0.1(3) | -1.5±0.5 | 0.9 | 11(2) | 29.17±0.5 | 19.40(1) | 1 | 0.476 | 0.289 | 0.012 |
| J174540.88–290328.9 | midM dMe? | ... | 36±10 | 0.6(4) | -2.2±0.7 | 1.6 | 7(3) | 29.40±0.9 | 20.02(1) | 1 | 0.518 | 0.195 | 0.017 |
| J174545.65–285621.7 | midM dMe | ... | 70±14 | 0.2(3) | -2.1±0.5 | 1.1 | 9(2) | 29.12±0.6 | 18.62(1) | 1 | 0.519 | 0.114 | 0.016 |
| J174548.61–290522.4 | lateG? | ... | 273±22 | 0.4(2) | -2.0±0.5 | 1.4 | 6(2) | 30.21±0.7 | 17.74(1) | 1 | 0.516 | 0.014 | 0.019 |
| J174549.18–285557.4 | F/G | ... | 89±13 | 0.3(3) | ... | 1.4 | 6(1) | ... | 17.28(1) | 1 | 0.980 | 0.598 | 0.059 |
| J174552.92–290358.8 | lateG? | ... | 831±33 | 0.3(2) | -2.3±0.5 | 1.4 | 4(2) | 30.39±0.7 | 16.12(1) | 1 | 0.431 | 0.096 | 0.015 |
| J174558.23–285644.3 | early/midK | ... | 185±22 | 0.4(1) | -2.3±0.4 | 1.5 | 6(1) | 29.85±0.7 | 17.79(1) | 1 | 0.536 | 0.114 | 0.019 |
| J174559.56–285435.8 | G/K | ... | 501±34 | 1.5(2) | -3.5±0.6 | 3.2 | ... | 30.04±0.9 | 20.16(4) | 1 | 0.575 | 0.506 | 0.017 |
| J174607.52–285951.3 | CV-B | cv | 3539±63 | 0.7(4)† | -0.1±0.9 | 1.9 | 8(3) | 31.25±0.9 | 21.75(3) | 1 | 0.430 | 0.007 | 0.013 |

^aChamPlane IDs have prefix ChOPS...^bSee Table 4 for explanation of spectral type classification.^cAdditional classification of source type. q: qLMXB candidate, by: BY Dra candidate, rs: RS CVn candidate, tt: T Tauri, cv: CV.

^dBackground subtracted net counts in the Bx band (0.3–8.0keV). *This source has SNR<3.

^eHydrogen column density N_H in units of 10^{22} cm^{-2} estimated from spectral fit. True value may be higher by ~ 0.2 , see text. † Objects with ‘?’ spectral type and CVs have N_H estimated from QCCD analysis.

^flog of the ratio of unabsorbed flux in S_C band 0.5–2.0keV to unreddened optical R band flux ($\text{ergs cm}^{-2} \text{ s}^{-1} (1000\text{\AA})^{-1}$)

^gThe distance in kpc. Error $\approx 60\%$.

^hlog of X-ray luminosity in S_C band (ergs s^{-1})

ⁱNM—number of optical matches found within 95% confidence (2σ) error circle of this X-ray source.

^j‘Srch’: the combined 95% X-ray and optical position error circle (arcsec) used to search for optical matches. ‘Offset’: the positional offset in arcsec between X-ray and optical position. ‘ P_{Rn} ’: random match probability given error circle size and measured local optical projected surface density.

3.2. Quantile Analysis

For stars with low signal-to-noise ratio optical spectra we assign in Table 5 a non-classification to the object ‘?’. In order to place constraints on N_H for these sources, and for the CVs, whose optical spectra are not well-modelled by single-temperature blackbodies, we utilize X-ray quantile analysis. Objects for which this has been carried out are marked with a ‘†’ in Table 5. Quantile analysis was first presented in Hong, Schlegel & Grindlay (28). It allows us to derive X-ray spectral information despite low source counts. It involves placing sources on an X-ray color-color diagram by the median and quartile energy fractions of their source counts. As defined by H04, any general quantile Q_x is calculated as:

$$Q_x = \frac{E_{x\%} - E_{lo}}{E_{up} - E_{lo}} \quad (1)$$

where $E_{x\%}$ is the energy below which the net counts is $x\%$ of the total number of counts between E_{lo} and E_{up} ; we select $E_{lo}=0.3$ and $E_{up}=8.0$ keV (B_X band) for our analysis. We plot the ratio Q_{25}/Q_{75} against $\log_{10}[m/(1-m)]$ ($m(\equiv Q_{50})$ is the median). For a given spectral model, we overlay a grid of column density N_H and model parameter—we interpolate to find a value for N_H . The grid shape is dependent on the *Chandra* ACIS response function for the ObsID considered.

Figure 4 shows QCCD plots for ObsID 53392, which includes CV-B (detected with ~ 3500 counts in this ObsID) and ObsID 945, which includes all three CVs we have detected in the *Chandra* fields considered in this paper. We use a thermal bremsstrahlung model to construct the grids shown in this case.

3.3. Extinction Model for the Galaxy

We require a method of deriving luminosity for our sources and so need a way of estimating their distances. Recently, Drimmel & Spergel (17) (hereafter D01) constructed a three-component model for the dust distribution in the Galaxy. This is used via a FORTRAN code (16, hereafter: D03) to derive the extinction, A_V as a function of distance from the Sun over the whole sky. The spatial resolution on which values of A_V can be measured is ~ 20 arcmin. Figure 5 shows the run of A_V with distance for each field in this paper. After fitting the optical spectra or using quantile analysis to derive extinction values A_V , we utilize the model of D01 to derive distances to all sources in this paper. The values listed in Table 5 are *not* corrected for the overestimate in A_V . As a check on the results, the spectral fit scaling factor R^2/d^2 allows us to derive a radius which we compare with expected values for stars of given spectral type and M_V (e.g. 10).

The code has a ‘rescaling’ option to account for small-scale variations and clumping in the dust density that are smoothed over by the model. This is based on a factor dependent on the residuals between the COBE observed flux at $240\mu\text{m}$ and the model prediction for the same. It was found that for all fields, using the rescaling option in the D03 code worked well in producing reasonable stellar radii within 50% of tabulated values (e.g. 10), with the exception of G347b, where radii were systematically a factor of four to five times higher.

For G347b we derive $A_V(d)$ using extracted emission spectra of Galactic molecular CO (from the survey of 11) and 21cm HI diffuse gas (data taken from the Southern Galactic Plane Survey, 60) to derive the column density of molecular and atomic hydrogen respectively, thus N_H via $N_H = N_{HI} + N_{H_2}$ and so A_V . The HI data has a resolution of $\sim 1'$, but for this analysis was smoothed to $3'$ resolution with $2.7'$ spacing. Emission from CO was assigned a distance based on line-of-sight velocity, splitting the near/far ambiguity based on the latitude of observation, and using the Galactic rotation curve of Brand & Blitz (8). We assumed a FWHM layer thickness for HI of 220pc (14), and for CO of 120pc (11). Emission beyond the terminal velocity cutoff was redistributed in a Gaussian below the cutoff with the Gaussian dispersion equal to the cloud-cloud velocity dispersion: $\sigma(\text{CO}) = 4 \text{ km s}^{-1}$, $\sigma(\text{HI}) = 8 \text{ km s}^{-1}$. We assume an atomic hydrogen spin temperature of 140K. We performed this calculation along two lines of sight—in Galactic coordinates these are at (l, b): 347.375, -0.75 and 347.375, -0.875 (positions 1 and 2 respectively). Figure 5, right-hand panel shows the resultant A_V versus distance plots for field G347b, labelled position 1 and position 2. We were unable to perform the same derivation for the other fields as the three Galactic Center fields (SgrA \star , SgrB2 and GalCA) are too close to the Galactic plane to easily assign distances to molecular emission, and for field J1655 the HI data available was not at high enough resolution to accurately run the calculation.

3.4. Calculating X-ray Fluxes

We calculate unabsorbed X-ray fluxes for all sources from their net count rates using *sherpa*³. For simplicity, we assume that the X-ray radiation produced by the majority of objects in our sample will be emission from a hot ($T > 10^6 \text{ K}$, $kT > 0.1 \text{ keV}$) coronal plasma. To calculate fluxes in the hard (H_C) and soft (S_C) bands for each star in our sample we thus adopt a simple single-temperature MEKAL model⁴ (bremsstrahlung emission of an optically thin, thermal plasma with metal absorption and emission lines; see 37) at 1keV and use the

³<http://cxc.harvard.edu/sherpa/threads/index/html>

⁴Model: xsmekal in sherpa

N_H value listed in Table 5. §3.4 below discusses the uncertainty introduced by our choice of spectral model on our results for X-ray flux. We derive X-ray luminosities via $L_x = 4\pi d^2 F_x$ ergs s⁻¹. The X-ray to optical flux ratio is calculated via:

$$\log(F_x/F_R) = \log(F_x) + 0.4R + 5.765 \quad (2)$$

and

$$\log(F_x/F_V) = \log(F_x) + 0.4V + 5.426 \quad (3)$$

where we have assumed a square optical filter transmission function of width 1000Å, centered on the filter’s quoted central wavelength, with an underlying A0 stellar spectrum to calculate the constants. Note that the overestimate in N_H from § 3 carried through results in $\Delta \log(F_x/F_V) = +0.3 - +0.5$ and $\Delta \log(L_x) \sim -0.3$. The exact correction depends on the object’s initial N_H . This is *not* incorporated in the results given in Table 5.

3.5. Error Analysis

The primary source of error in our analysis is the calculation of $E(B-V)$ —this has three components. Firstly, there is the uncertainty in assigned T_{eff} values ($\pm \sim 500K$). Secondly, from systematic errors in the flux calibrated spectra (from the extraction and calibration processes). The flux calibration error ranges from ~ 10 to 60%—estimated by comparing repeat observations of stars observed on multiple nights. This was the case for moderate and also high S/N spectra. Variations were evident in spectra both within a night as well as from night to night. Thirdly, errors introduced by our spectral fitting code. We estimate this by selecting 17 standard star spectra (types M5 V through A7 V) from the catalog of Jacoby et al. (33), applying a range of fake values of interstellar reddening ($E(B - V) = 0.3-4.0$) with the *fm_unred* command in IDL⁵ and then attempting to retrieve this fake reddening with our spectral fit code. The ‘error’ on the returned value $\Delta E(B - V) \approx 50\%$ at $E(B - V) \approx 0.3$, ranging down to $\approx 6\%$ at $E(B - V) \approx 1.3$ (independent of spectral type). We linearly interpolate this trend to calculate the uncertainty produced by the fitting process at any $E(B - V)$. The quoted error in column density N_H in Table 5 in column 5 combines all these three sources.

Errors quoted in Table 5 for $\log(F_x/F_R)$ and $\log(L_x)$ incorporate uncertainty in N_H , in the X-ray count rate and photometric error in the R magnitude (a relatively small contribution). The choice of X-ray spectral model (1.0keV MEKAL) also contributes to our

⁵<http://idlastro.gsfc.nasa.gov/>

uncertainty. Using a power law model with spectral index $\Gamma=1.7$ or a MEKAL (kT=2.0 keV) reduces the S_C band flux by between 10% (at $N_H \approx 0.2 \times 10^{22} \text{ cm}^{-2}$) and 50% (at $N_H \approx 2.0 \times 10^{22} \text{ cm}^{-2}$). A MEKAL model with kT=0.5 keV creates a similar *increase* in the S_C band flux. Thus the errors quoted in $\log(F_x/F_R)$ and $\log(L_x)$ should be considered as lower limits.

Using the model of Drimmel & Spergel (17) introduces error in our distance calculation. Results for d derived from this model for Galactic longitudes $|l| < 20^\circ$ are likely to suffer from significant systematic uncertainty as true structure in the absorbing interstellar medium is significant in this part of the Galaxy and is poorly modeled in the code. The fact that fields SgrB2 and GalCA ($\sim 0.5^\circ$ apart of the sky) are indistinguishable on this figure and the curve for field SgrA \star (which is only $\sim 12'$ away) is significantly different is almost certainly a resultant artifact, not a real trait of these two three fields. The combined error from spectral fit and dust model (estimated by comparing variation in A_V across the *Chandra* field of view) in the distances we derive is typically $\lesssim 60\%$. We adopt 60% as the error on the distances that we quote in Table 5. This carries through to error in X-ray luminosity and optical absolute magnitudes.

4. Results

Table 5 presents our spectral results. Optical photometry comes from data from our 2000 and 2003 CTIO Mosaic runs (see 70). For each source in Table 5 we list the ChaMPlane IAU optical source ID (column [1]). Readers desiring to find detailed X-ray counterpart properties can readily search our online X-ray database⁶ using the optical source ID for coordinates. We then give the source properties: spectral classification (column [2]), net X-ray source counts in the B_X band (column [3]), the hydrogen column density N_H as derived from our fitting technique or quantile analysis (column [4]), the unabsorbed X-ray to R -band flux ratio in the S_C band, adopting a 1.0 keV MEKAL X-ray spectral model (column [5], see § 2 for band definitions). Although subsequent analysis is performed on a derivation of $\log(F_x/F_V)$ for easier comparison with the literature, the actual numbers do not differ significantly from those listed for $\log(F_x/F_R)$. In addition, since $\sim 10\%$ of our objects are undetected in V , we can give a value for more sources by presenting this information instead. The distance and the derived absolute visual magnitude M_V are in columns [6] and [7]. We then give X-ray luminosity, followed by the optical R magnitude and the number of optical sources found to match the same X-ray position (columns [8], [9]

⁶http://hea-www.harvard.edu/ChaMPlane/database_xray.html

and [10]). Column [11] gives the X-ray 2σ search radius size in arcseconds and column [12] gives the offset of the optical position in arcsec from the center of the X-ray error circle. Column [13] gives the expected number of optical sources that should fall in an error circle of this size by chance, given the observed surface density of stars within 1 arcmin of the X-ray position on the Mosaic image. For almost all objects in Table 5 one optical source matches the X-ray position, however, in the J1655 field, ChOPSJ165407.44–394542.7 and J165350.37–394621.9, in the G347b field ChOPSJ171524.21–395950.9 and in the SgrB2 field ChOPSJ174719.59–282204.9, J174633.29–282512.7 and J174634.65–282721.1 are all one of multiple matches to single X-ray sources. In the case of ChOPSJ165350.37–394621.9 in J1655 we have a spectrum of the other match—we select the M-type star as the more likely X-ray emitting candidate over the G-type alternate. The ‘Classification’ column follows the scheme: mid G represents G4–G6, late G: G6–G8, F/G: F8–G2 and so on. A question mark placed next to a classification indicates that the uncertainty in spectral type is greater so mid G? means G3–G7 and F/G? means F7–G3. A star classified as G? means G0–G9 (and equivalently for other types).

4.1. Cataclysmic Variables

The full list of matches between our X-ray and optical source lists having $H\alpha - R < -0.3$, $V < 23$ and an optical signal to noise ratio > 1.4 is given in Table 6 below⁷. We restrict $H\alpha - R$ based on the work of Szkody et al. (58) who find that only 17% of their sample of CVs from the Sloan Survey have an $H\alpha$ equivalent width below 28\AA in emission (i.e. have $H\alpha - R > -0.3$). We can use spectra to rule out 4 of these as dMe, normal or T Tauri stars. The objects: ChOPSJ174559.18–290418.9 in field SgrA \star and ChOPSJ165335.32–393715.9 in field J1655 had no optical spectra taken in any ChaMPlane observing run and so remain uncertain CV candidates.

Qualitative analysis of the remaining spectra reveals two clear CV candidates in the GalCA field from the LDSS2 spectral sample (see Table 5, sources ChOPSJ174638.02–285326.2 and ...656.89-285233.9). Hereafter we refer to these as CV-A and CV-C respectively (see Figures 6a and 6c). Another source, ChOPSJ174607.52-285951.3 (hereafter, CV-B), was imaged with LDSS2 in the SgrA \star field, but the spectrum suffered from being on the edge of the slit and was not possible to extract. It was later re-observed by the IMACS instrument at Magellan—its IMACS spectrum is shown in Figure 6b. All three spectra show broad $H\alpha$ in emission. CV-A and CV-B also show emission lines of HeI.

⁷CV-C is included for its broad $H\alpha$ emission line.

Table 6. $H\alpha - R < -0.3$ Objects

| ChOPS ID | $H\alpha - R$ | R | Spectrum | $\log(F_x/F_R)$ |
|-----------------|---------------------|------|----------|-----------------|
| J1655 | | | | |
| 335.32-393715.9 | $-0.46(6)$ | 21.5 | None | $< -0.99^*$ |
| 422.01-395205.0 | $-0.39(2)$ | 19.6 | dMe | -1.5 ± 0.5 |
| GalCA | | | | |
| 638.02-285326.2 | $-0.65(2)^\dagger$ | 20.2 | CV(A) | 1.2 ± 0.6 |
| 656.89-285233.9 | $-0.19(4)^\ddagger$ | 21.3 | CV(C) | < -2.3 |
| SgrB2 | | | | |
| 732.09-282033.8 | $-0.61(1)$ | 16.2 | T Tauri | -2.7 ± 0.5 |
| 708.21-282724.8 | $-0.38(1)$ | 19.8 | G? | -2.5 ± 0.5 |
| SgrA | | | | |
| 511.51-290236.8 | $-0.31(1)$ | 19.2 | dMe | -2.5 ± 0.9 |
| 559.18-290418.9 | $-0.6(1)$ | 22.7 | None | -1.5 ± 0.5 |
| 607.52-285951.3 | $-0.61(4)$ | 21.8 | CV(B) | -0.1 ± 0.9 |

Note. — Numbers in parentheses with $H\alpha - R$ value represent error in last quoted digit. *Undetected in S_C band—estimated upper limit to flux ratio. † This value of $H\alpha - R$ was recorded in 2000. In 2003 it had dropped to -0.182 . ‡ CV-C is included here despite having $H\alpha - R > -0.3$.

CV-B was previously detected by ROSAT Position Sensitive Proportional Counter (PSPC) observations of the GC regions (54), as their source ‘65,’ but without further identification possible at the time. It was found to have a count rate of 1.9 ± 0.3 cts ks^{-1} in the ROSAT band 0.1–2.4keV. Using the online PIMMS tool with an assumed thermal bremsstrahlung spectrum with $kT = 7.3$ keV and $N_H = 5 \times 10^{21}$ cm^{-2} from our QCCD analysis (Figure 4), this converts to a *Chandra* hard-band (2–8 keV) flux of $1.0 \pm 0.2 \times 10^{-13}$ $\text{erg s}^{-1} \text{cm}^{-2}$. From our *Chandra* data we estimate $0.64 \pm 0.15 \times 10^{-13}$ $\text{erg s}^{-1} \text{cm}^{-2}$, possibly indicative of some slight variability.

We use the QCCD results of Figure 4 to estimate by eye a plausible initial spectral model (CV-A and CV-B were detected in ObsID 945 with ~ 300 counts, CV-C has only ~ 26 counts). If we assume that a bremsstrahlung spectrum is representative of their X-ray emission, we can thus estimate their spectral properties (see Table 7). We present XSPEC⁸ fits for the two X-ray bright CVs (CV-A and CV-B) in Figure 7 below. We use a bremsstrahlung emission plus photon absorption model for the fit to each spectrum. CV-C has too few counts to provide adequate signal to noise for spectral fitting. The results we derive are shown in Table 7 below. For CV-A and CV-B, the quantile-derived parameters are in good agreement with the estimates from the XSPEC fits. For CV-C, we can only place weak constraints on N_H and kT , but the error bars are consistent with a typical CV spectrum of bremsstrahlung at ~ 2 –8keV. This is suggestive that these CVs are all dwarf novae (DN)—typically characterized by hot ($\sim 10^8$ K) hard X-ray spectra in quiescence (66). We note however, that the absolute magnitudes M_V for CV-A and CV-C are on the bright side for quiescent DN (3 and < 3.99 respectively).

The final tally of likely CVs is thus: 1 (possibly 2) in SgrA \star , 2 in GalCA and possibly

⁸<http://xspec.gsfc.nasa.gov/docs/xanadu/xspec/index.html>

Table 7. CVs With LDSS2 Spectra

| CV | ChOPS ID ^a | $H\alpha - R$ (mag) | FWHM ^b $H\alpha$ (Å) | EW ^c $H\alpha$ (Å) | XSPEC | | QCCD | |
|------|-----------------------|------------------------|------------------------------------|----------------------------------|--------------------|---------------|--------------------|------------|
| | | | | | N_H ^e | kT (keV) | N_H ^e | kT (keV) |
| CV-A | 638.02-285326.2 | -0.66(3) ^c | 26 \pm 3 | -48 \pm 5 | 1.0 \pm 0.2 | 8.9 \pm 4.6 | 1.4 \pm 0.3 | 9 \pm 3 |
| CV-B | 607.52-285951.3 | -0.63(4) | 24 \pm 3 | -81 \pm 7 | 0.5 \pm 0.03 | 7.3 \pm 0.9 | 0.7 \pm 0.4 | 8 \pm 1 |
| CV-C | 656.89-285233.9 | -0.20(4) | 31 \pm 3 | -60 \pm 10 | ... | ... | >1.4 | ... |

^aAbbreviated IDs: prefix ChOPSJ174...

^bFull width at half maximum intensity of the $H\alpha$ line

^cEquivalent width of the $H\alpha$ line.

^dAs of 2000. In 2003 $H\alpha - R$ was measured at -0.194.

^e N_H in units of 10^{22}cm^{-2}

1 in the J1655 field. This latter object lies outside the main ACIS-S chip (S3) and its neighboring S4 chip—the large error circle size in which it is found means that even when looking exclusively at objects with $H\alpha - R < -0.3$ in the field, the probability it is a random match is high (>20%). We consider this a low probability CV candidate.

4.2. Stellar X-ray Sources

In order to compare our sample of stellar X-ray sources with other surveys we construct their luminosity functions and assemble an X-ray to optical flux ratio histogram.

Since our survey is flux limited, we correct for incompleteness with the $1/V_{max}$ method of Schmidt (50). In this method, each source contributes 1 over the maximum volume in which it could have been detected in our survey to its bin in the cumulative luminosity histogram. This maximum volume is calculated in the following way: given one ACIS pixel in a *Chandra* observation, with a known limiting (3σ) count rate for detection (and thus limiting flux, given a spectral model) we can calculate a maximum distance d_{max} , that an object of known luminosity could be placed and still be detected. This defines a pyramidal volume given by the size of the pixel on the sky. To calculate the full volume, we simply repeat this process across the whole field of view, using the 3σ count rate limit at each point and sum the resulting volume elements together. To speed the calculation up we re-bin each *Chandra* image by a factor 80.

We divide the sources into intermediate (early F to late G) and late (G/K to M) types, and plot the resultant, V_{max} -corrected luminosity functions in Figure 8 below. We use luminosity calculated in the ROSAT band (0.1–2.4keV) for ease of comparison with past surveys, despite the mismatch in bandpass more suitable to our reddened fields. We overplot comparison luminosity functions of main sequence stars (from the volume limited survey of 51), and young main-sequence stars from the ROSAT surveys of the Hyades (age < 1Gyr 57) and the Pleiades (age $\sim 10^8$ yrs 38). We convert their quoted luminosities into the 0.1–2.4 keV band using the online PIMMS tool⁹. Since in § 3.1 we concluded that the spectral fit N_H overestimates the true value, for this comparison we generate luminosities with N_H reduced by $0.2 \times 10^{22} \text{ cm}^{-2}$, and consequently *distances* reduced appropriately given the D01 model.

In Figure 9 we plot a comparative histogram of the X-ray to optical flux ratio (V -band flux), i.e. $\log(F_X/F_V)$. Again we utilize the reduced N_H values to generate X-ray rate-to-flux conversions to calculate the X-ray fluxes, and de-redden the optical magnitudes. We

⁹<http://xc.harvard.edu/toolkit/pimms.jsp>

overplot the samples of Schmitt & Liefke (51), Stern et al. (57) and Micela et al. (38), scaled so that the total area under each curve is the same for all histograms within a plot.

4.3. Candidate Low Mass X-ray Binary

A quiescent low-mass X-ray binary (qLMXB) system consisting of a black hole or neutron star and a main sequence star will most likely show strong $H\alpha$ in emission in its optical spectrum. Some CVs and qLMXBs have sub-giant companions; these are more likely to be detected in our reddened sample. Since the only objects showing $H\alpha$ in emission in this sample are either CVs or T Tauri stars (and identified as such in Table 5), we look to the example of GRO J165540 (69; 26; 3) a known qLMXB, soft X-ray transient system, consisting of an F3–6IV sub-giant star secondary and an accreting black hole primary. This system shows $H\alpha$ in absorption in quiescence: the secondary star is luminous enough to hide the emission line produced by the accretion disk. Our spectral classification is not precise enough to ascertain the luminosity classes of stars in the sample, so to find analogs to this system we search for stars with spectral type earlier than K, with absolute magnitude M_V more than 2σ higher than that expected for a main sequence star of that type (see Table 4). We then look for stars with $\log(F_X/F_R)$ (S_C band) more than 2σ greater than that seen in sub-giant stars in the survey of Hünsch et al. (1998a). In Table 5 we flag the one candidate: ChOPSJ165408.14–395636.1 that we find after this search. Figure 10a presents the LDSS2 spectrum. This is only a very tentative classification—it is also possible that this object is an active binary of RS CVn type (Hall(1976)). We note that on the basis of its spectrum, and X-ray properties in quiescence alone, GRO J1655–40 (see Figure 10b) could be mistaken for an RS CVn system. Further variability analysis and detailed spectral followup is necessary to rule out this object as a black hole or neutron star binary system.

5. Discussion

5.1. Stellar Coronal Emission

We have discovered a large sample of stellar coronal emission sources in our survey fields. Recent studies, (for example, 59; 53) have shown that flux-limited X-ray surveys of the Galaxy (within the disk) will naturally sample preferentially from the youngest stellar populations present in the Galactic disk, owing to the known decline of stellar X-ray emission with age (63). Figures 7 and 8 show that the objects discovered in our survey are somewhat elevated in their X-ray emission, hence one explanation is that they are young. In this

picture, the luminosity functions in Figure 8 are possibly explained by a composite of local (old) and younger population (Hyades and Pleiades age) stars. However, the presence of very luminous objects ($\log(L_X) > 30$) suggests an additional component, as does the excess of objects at high $\log(F_X/F_V)$ in Figure 9.

The first possibility is that we are detecting an even younger population, in other words a component of pre-main-sequence (pre-MS) stars. Results from ROSAT and the COUP (21) show that T Tauri stars (weak-lined and classical) can have X-ray luminosities in excess of 10^{30} erg s $^{-1}$, and in some cases greater than 10^{31} erg s $^{-1}$. Since our survey covers fields at low Galactic latitude ($|b| < 3^\circ$), and since the scale height of stars also increases with age (67), this is a likely source of X-ray active objects. To further test the likely pre-MS content of our survey, we examined the near-infrared (near-IR) colors of ChaMPlane objects in this paper (using online data from the 2MASS survey, 56). In Figure 11 we present a plot of $J - H$ versus $H - K_S$ colors obtained in this way. We found 92 2MASS matches to our 136-object source-list. Overlaid on the plot are the locus of Main-Sequence stars and giants from Bessell & Brett (5), and a reddening vector created using the near-IR extinction relation of Nishiyama et al. (42). Objects below the line are candidate infrared excess (T Tauri) young stars (following the work of 35)—a total of between 36 and 56, or 39–61% of sources (the range is due to the 2MASS photometric uncertainty). It is also possible for T Tauri stars to be found above the line—this component is not possible to establish without high resolution spectroscopy to measure Lithium 6708Å absorption equivalent widths.

The other alternative explanation for the X-ray active objects are active binaries (ABs) of either RS CVn or BY Dra (7) type, or cataclysmic variables. The studies of Dempsey et al. (12) and Dempsey et al. (13) showed that $\log(L_X)$ can range up to 32 for RS CVn and BY Dra systems, with $\log(F_X/F_V)$ up to -1.0. CVs also typically have $\log(F_X/F_V) \sim -3$ – $+1$ (64), however the lack of broad H α argues against CVs unless they have sub-giant companions. To estimate the likely contribution of ABs to our sample, we use a method similar to that used by Grindlay et al. (25). We define a maximum distance at which an AB would have been identified given the optical and X-ray detection limits of our survey. Given some model for the distribution of ABs in the Galaxy, we can predict the number we expect to detect in the corresponding volume.

The detectability of a given AB in our *Chandra* observations is determined by the detection limit of the observation, the hydrogen column intervening between the telescope and the object, its luminosity and the spectral model assumed for its emission.

To quantify the *Chandra* sensitivity in the calculation, we extract the count rate limit for each observation across the field of view. For simplicity we use an average value across the detector for each field in the B $_X$ band. We derive the hydrogen column density N_H

encountered as a function of distance using the D01 calculation of A_V in the direction of the aimpoint of each field. As a simple approximation, we assume that ABs are distributed in the Galaxy with some exponential scale height h in the z direction: $n_{CV} \propto \exp^{-d(\sin|b|)/h}$, with n_{AB} the AB space density and b the galactic latitude. This is probably a reasonable assumption for the regions surveyed in this paper (provided we are only considering the distribution within ~ 3 kpc of the Solar neighborhood). Following Grindlay et al. (25), we consequently utilize the formalism of Tinney et al. (61) in constructing an effective detection volume V_{eff} , as defined by d_{max} :

$$V_{eff} = \Omega (h/\sin|b|)^3 [2 - (\chi^2 + 2\chi + 2) \exp(-\chi)] \quad (4)$$

where $\chi = d_{max}(\sin|b|)/h$ and Ω the solid angle subtended by the ACIS field of view. V_{eff} corrects the *geometric* volume in which we search for the non-uniformity of the AB space density. d_{max} is the limiting distance at which a AB at a luminosity of $10^{32.0}$ ergs s^{-1} (the maximum value for ABs found by ROSAT 12) could be detected in the *Chandra* observation considered. For the ACIS-S observation J1655, we use the full $8' \times 8'$ field of view to calculate Ω . The GalCA pointing overlaps the SgrA* field of view, so this field only adds three-quarters of the full ACIS-I solid angle to the area of sky surveyed. The number of ABs we might expect to be present in such a volume is then $N_{AB} = n_{AB} \times V_{eff}$.

Following the conclusions of Sciortino et al. (53) we adopt an AB scale height of $h = 250$ pc, and a local space density $n_{AB} = 3.7 \times 10^{-5}$ pc^{-3} (19). For the X-ray spectral model, we adopt a MEKAL $kT = 1.0$ keV single temperature model. To model the detection rate of ABs, we populate each volume uniformly with a randomly distributed sample of 10^4 ABs from 0 pc up to d_{max} as determined for each field. Each is assigned an X-ray luminosity and absolute visual magnitude, sampling randomly from the data of Dempsey et al. (12) and Dempsey et al. (13), using *only* objects they classify as RS CVn or BY Dra type. This enables us to determine if an object is luminous enough in X-rays and apparent visual magnitude to be detected in our survey (using an assumed detection limit of $V=21$ for an object to be spectrally classified). Combining the detection rate derived with the predicted number of ABs in each volume, we predict between 13 and 14 ABs found in our survey. Based on absolute visual magnitude and high $\log(F_X/F_{opt})$ ratio¹⁰, we flag our best AB candidates in Table 5.

Our stellar coronal source sample appears likely to be a mix of both local, young-MS and pre-MS stars, and a component of coronally active binaries: RS CVn and BY Dra

¹⁰RS CVn: M_V more than 2σ less than that expected for a main sequence star of that spectral type and $\log(F_X/F_R) > -5.0$. BY Dra: M_V consistent with main sequence, $\log(F_X/F_R)$ more than 2σ greater than that expected for its spectral type (32)

type. To specifically compare the stars of these types in our sample with those found by ROSAT would require significantly improved spectral, variability and orbital analysis to more precisely classify our objects and tease out the contributions of age, metallicity, and binarity that might also be contributing to the observed differences the luminosity and X-ray to optical flux ratio.

5.2. Constraints on the Galactic CV Density

A main aim of the ChaMPlane survey is to investigate what constraints we can place on the local CV space density. We follow a method similar to that described in § 5.1.

For the *Chandra* sensitivity in the calculation, we use a single value for the *Chandra* H_C band, averaging over a $5'$ radius circle centered on the aimpoint. For the X-ray spectral model, we adopt a $kT = 8$ keV bremsstrahlung emission spectrum as “typical” for dwarf nova CVs (66). In this case, d_{max} is the limiting distance at which a CV at a luminosity of $10^{32.5}$ ergs s^{-1} (the maximum value for CVs found by ROSAT 64) could be detected in the *Chandra* observation considered.

We adopt a scale height of $h = 200$ pc, and following the conclusions of Grindlay et al. (25) among others, we adopt a local space density $n_{CV} = 1 \times 10^{-5}$ pc^{-3} . We populate each volume uniformly with a randomly distributed sample of 10^5 CVs from 0 pc up to d_{max} as determined for each field. We assign each fake CV an X-ray luminosity (in the H_C band) and X-ray to optical flux ratio $\log(F_x/F_V)$: we sample L_x X-ray data as collected by Grindlay et al. (25), originally presented in Hertz et al. (27), and the ROSAT survey (see: 64; 52), to construct distributions in L_x and $\log(F_x/F_V)$ from which we randomly sample. We assume that these two parameters are uncorrelated (a simple scatter plot shows this to be the case for the 49 CVs in the ROSAT sample). For a bremsstrahlung X-ray spectral model at 8keV, the luminosity in the ROSAT band 0.1–2.4keV and our H_C band is approximately the same. We then derive an apparent V magnitude and observed X-ray flux. We set our photometric detection limit at a V magnitude of 23—the faintest that we could have detected a CV via its $H\alpha - R$ color. The number of CVs *expected* to be present in each field is given in Table 8 as ‘CV_{32.5}’ (column 5). The X-ray detection and optical identification percentages of these objects are given in columns 6 and 7. The resultant number of predicted CV detections is given as ID_{32.5}. Since the optical detection limit is reached at only ~ 2 kpc, the optical percentage quoted below is essentially equal to the combined ‘X-ray-and-optical’ detection percentage.

It is apparent that there is an excess of CV candidates over the number predicted by

our simulation. In SgrA \star and GalCA fields considered in isolation there are a factor ~ 10 –70 too many. However, summing over all fields we find between 3 and 5 detected, with 0.95 ± 0.08 predicted. A simple χ^2 table shows that this result is statistically significant at $\sim 92\%$ confidence. What factors are contributing to the discrepant estimation of the CV detection rate?

We have assumed that a single relationship between A_V and distance is applicable over each $16' \times 16'$ *Chandra* field of view yet extremes in the level of extinction are observed directly in infrared images of the SgrA \star and GalCA fields (see e.g. 36). The D01 model overlooks this small scale variability across each field. If there were some covering factor of higher-column-density gas and dust across each field or regions of significantly lower extinction, we would expect to alter the number of predicted CVs detected. However, a factor of ~ 15 decrease in the amount of extinction as a function of distance is necessary to produce the factor ~ 60 increase in the overall prediction for CV detections in GalCA, and at least a factor ~ 5 reduction is required to solve the discrepancy for SgrA \star . Although there is some great uncertainty in the dust model towards the Galactic Center this appears unlikely. Improvements to the dust model are vital to understand if this effect is more significant.

We included no radial component in our model CV space distribution yet it is likely that there is some increase in the space density of CVs as we approach the Galactic Center (see, e.g. 46). Thus we are underestimating the true number of CVs present in each volume, before we apply our detection criteria. This may only be a minor correction, since our optical detection and spectroscopic identification limit restricts us to looking in the nearest ~ 2 kpc to the Sun. Some additional work on improving how we model where the CVs are in our volume, and how many we expect to be in this volume is important to establish by how much we are underestimating N_{CV} . Such a modification would appear to be most necessary for the two fields closest to the Galactic Center: SgrA \star and GalCA.

We restricted the detection solid angle to the inner $5'$ of the *Chandra* field of view. Including the outer parts of the detector (or for ACIS-S including the other S-chips) increases the detection area by a factor ~ 3 . However, the X-ray count rate limit beyond $5'$ is lower (on average by a factor ~ 2) than at the aimpoint, which although not affecting optical detectability, means the increase in predicted CV numbers would be small in comparison with other effects discussed above.

Patterson (private communication) recommends a smaller scale height $h=150$ pc on the basis of local CV surveys. Implementing this affects only field J1655 significantly and would reduce the *predicted* number of CVs by $\sim 20\%$ —further in line with our lack of CVs detected in this field.

At face value, our results suggest a higher in local value of the CV density, n_{CV} , although alternatively the excess of objects detected may simply represent fluctuations over a mean background rate. The parameter n_{CV} directly influences the predicted number of CVs in any given field. Our sample is too small to be used to argue strongly for a change, however the significance of the difference between the observed number of CVs and our predicted number certainly suggests an increase (by a factor $\sim 3-5$) is justified. Two recent studies find different values for n_{CV} . Rogel et al. (46) construct a Galaxy source-distribution model to predict CV detections found in ChaMPlane Galactic Anti-center fields, and find a value of 10^{-5} pc^{-3} provides the best fit to their results. However, Ak et al. (1) use a sample of 459 local Solar-neighborhood CVs to derive a value of n_{CV} a factor ~ 3 higher than this, which appears to validate our own findings. Thus it may indeed be that the value of n_{CV} is somewhat higher than our adopted value.

5.3. Resolving the Galactic Ridge X-ray Emission

The extended Galactic Ridge X-ray Emission observed throughout the Galactic Plane (GRXE, see e.g. 68) is the subject of disagreement over whether deeper, higher resolution observations in the X-ray band will eventually completely resolve all observed Galactic emission at this wavelength, or whether in fact there is a truly diffuse emitting plasma confined to the Galactic Plane. Ebisawa et al. (18) carried out deep, ~ 100 ksec X-ray observations of two fields in the Galactic Plane with *Chandra* and estimated that point sources contribute at most 10% of the total X-ray flux they observe in this region. They conclude that no faint, unobserved point source population could simultaneously match their observed logN–logS (number versus source flux) plots of point sources and the total GRXE flux, and hence there is a truly diffuse component to the GRXE. On the other hand, Revnivtsev et al. (47) show that, since the morphology of the GRXE very closely matches that of the Galactic near-infrared surface brightness, it must trace the stellar mass distribution of the Galaxy. They calculate the X-ray luminosity per unit stellar mass that this conclusion requires in order to match the observed flux of the GRXE. Together with the X-ray luminosity function of Sazonov et al. (48) they show that the X-ray emissivity per unit mass of the local Solar neighborhood X-ray source population extended to the whole Galaxy can easily account for the GRXE.

The probable types of the counterparts to our X-ray source population are active binaries ($\sim 10\%$ of the sample), CVs ($\sim 2\%$), YSOs (perhaps between 39 and 61%), with the remainder coronally emitting stars, either young main sequence or main sequence objects. Broadly and qualitatively this result agrees with the make-up of the Solar neighborhood

population as determined by Sazonov et al. (48). A more detailed comparison with their luminosity function is limited by two factors: 1) the fact that our survey is not complete in either magnitude/source flux space, or volume space, and 2) the lack of detailed source classification and hence a determination of the X-ray emissivity per stellar mass of our sources. However, our results suggest a significant contribution to X-ray emitting sources close to the Galactic Plane comes from pre-main sequence and young main sequence stars, which can have relatively high X-ray luminosities ($L_x \sim 10^{31}$ erg s⁻¹).

In order to make progress to address the conflict over the origin of the GRXE requires one or both of: deep X-ray observations (~ 1 Megasec 47) or accurate classification (via optical or infrared spectroscopy or X-ray spectral analysis) of the faint, hard X-ray source population present in many *Chandra* X-ray studies of the Galactic Plane (e.g. 41). Although our Galactic center pointing approaches the first requirement, it still falls somewhat short and is hindered by the large extinction towards this field ($\log(N_H) \approx 23.0$ cm⁻²). Since we use optical spectroscopy to classify targets, we are necessarily limited to relatively bright ($R \lesssim 21$), nearby objects and as a result preferentially observe soft X-ray emitting, more unabsorbed sources. A forthcoming ChaMPlane paper (Hong et al 2008, in preparation) will utilise very deep (~ 1 Megasec) *Chandra* observations of the Galactic center together with our quantile analysis technique to classify faint point sources to directly consider the origin of the GRXE.

6. Conclusion

We have carried out optical and X-ray spectral analysis on a sample of X-ray detected optical sources in the Galactic plane, using a combination of optical spectral fitting and quantile X-ray analysis to obtain the extinction $E(B - V)$ and hence A_V and hydrogen column density, N_H towards each object. We combine these estimates with the work of Drimmel & Spergel (17) who present a three-dimensional dust model of the Galaxy in order to derive A_V as a function of distance in any direction, and thus further derive a distance to each object.

We present the discovery of a population of stellar coronal emission sources, detected by *Chandra* in five fields towards the Galactic bulge. These are likely a mix of young stars, of roughly Hyades and Pleiades age, as well as some pre-MS stars, and a component of RS CVn or BY Dra type. We find no strong evidence that we have sampled from stars with significantly different properties from local, similarly active stars. We report the properties of the most probable RS CVn and BY Dra-type candidates from our sample, and identify one possible qLMXB candidate also. We note that this latter object could instead be an RS

CVn system. High resolution optical spectra can make this clear.

We report the discovery of three X-ray detected CVs in the direction of the Galactic Center. All three are consistent with having an X-ray spectrum consisting of bremsstrahlung at $kT \approx 8\text{keV}$, and are within ≈ 2 kpc of the Sun. An additional 2 CVs are indicated by our photometry and X-ray data, and can be tested with optical spectroscopy.

The number of CVs detected in our survey is consistent with a local CV space density of $\sim 10^{-5} \text{ pc}^{-3}$, and a scale height $\sim 200\text{pc}$, but is suggestive of a larger local value or strong radial gradient. However, there is considerable uncertainty in the model we use to predict extinction as a function of distance and hence derive the number detected in our survey. Although the numerical uncertainty in the model appears to be a factor of ~ 3 (see Figure 5), cf. the required factor $\sim 5\text{--}15$ to rectify the discrepancies seen in the GalCA and SgrA fields, it is possible that true variations in the distribution of dust in the Galaxy might be able to explain this. Further work on better modelling the Galactic dust distribution and CV content of our fields is desirable to improve our constraints.

The author would like to thank John Silverman for collecting the LDSS2 spectral data during the 2001 run; JEG collected the LDSS2 spectra in the 2002 run. We also thank the two anonymous referees and Eric Feigelson whose suggestions considerably improved the manuscript. This research has made use of the SIMBAD database, operated at CDS, Strasbourg, France and the NASA Astrophysics Data System. This work is supported in part by NASA/*Chandra* grants AR1-2001X, AR2-3002A, AR3-4002A, AR4-5003A, AR6-7010X, NSF grant AST-0098683, and the *Chandra* X-ray Center. We thank NOAO for its support via the Long Term Survey program.

REFERENCES

- Ak, T., Bilir, S., Ak, S., & Eker, Z. 2008, *New Astronomy*, 13, 133
- Andrillat, Y., Jaschek, C., & Jaschek, M. 1995, *A&AS*, 112, 475
- Bailyn, C. D., Orosz, J. A., McClintock, J. E., & Remillard, R. A. 1995, *Nature*, 378, 157
- Bertout, C. 1989, *ARA&A*, 27, 351
- Bessell, M. S. & Brett, J. M. 1988, *PASP*, 100, 1134
- Bessell, M. S. 1991, *AJ*, 101, 662

- Bopp, B. W. & Fekel, Jr., F. 1977, *AJ*, 82, 490
- Brand, J. & Blitz, L. 1993, *A&A*, 275, 67
- Carquillat, M. J., Jaschek, C., Jaschek, M., & Ginestet, N. 1997, *A&AS*, 123, 5
- Cox, A. N. 2000, *Allen's astrophysical quantities* (*Allen's astrophysical quantities*, 4th ed. Publisher: New York: AIP Press; Springer, 2000. Edited by Arthur N. Cox. ISBN: 0387987460)
- Dame, T. M., Hartmann, D., & Thaddeus, P. 2001, *ApJ*, 547, 792
- Dempsey, R. C., Linsky, J. L., Fleming, T. A., & Schmitt, J. H. M. M. 1993, *ApJS*, 86, 599
- . 1997, *ApJ*, 478, 358
- Dickey, J. M. & Lockman, F. J. 1990, *ARA&A*, 28, 215
- Dopita, M. A. & Sutherland, R. S. 2003, *Astrophysics of the diffuse universe* (*Astrophysics of the diffuse universe*, Berlin, New York: Springer, 2003. Astronomy and astrophysics library, ISBN 3540433627)
- Drimmel, R., Cabrera-Lavers, A., & López-Corredoira, M. 2003, *A&A*, 409, 205
- Drimmel, R. & Spergel, D. N. 2001, *ApJ*, 556, 181
- Ebisawa, K., et al. 2005, *ApJ*, 635, 214
- Favata, F., Micela, G., & Sciortino, S. 1995, *A&A*, 298, 482
- Favata, F. & Micela, G. 2003, *Space Science Reviews*, 108, 577
- Getman, K. V., et al. 2005, *ApJS*, 160, 319
- Güdel, M. 2004, *A&A Rev.*, 12, 71
- Gray, D. F. 1992, *The observation and analysis of stellar photospheres* (*Cambridge Astrophysics Series*, Cambridge: Cambridge University Press, 1992, 2nd ed., ISBN 0521403200.)
- Grindlay, J., et al. 2003, *Astronomische Nachrichten*, 324, 57
- Grindlay, J. E., et al. 2005, *ApJ*, 635, 920
- Harmon, B. A., et al. 1995, *Nature*, 374, 703

- Hall, D. S. 1976, in IAU Colloq. 29, Multiple Periodic Variable Stars, ed. W. S. Fitch (Dordrecht: Reidel), 287
- Hertz, P., Bailyn, C. D., Grindlay, J. E., Garcia, M. R., Cohn, H., & Lugger, P. M. 1990, ApJ, 364, 251
- Hong, J., Schlegel, E. M., & Grindlay, J. E. 2004, ApJ, 614, 508
- Hong, J., van den Berg, M., Schlegel, E. M., Grindlay, J. E., Koenig, X., Laycock, S., & Zhao, P. 2005, ApJ, 635, 907
- Houk, N., Swift, C. M., Murray, C. A., Penston, M. J., & Binney, J. J. 1997, in ESA SP-402: Hipparcos - Venice '97, 279–282
- Howarth, I. D. 1983, MNRAS, 203, 301
- Hünsch, M., Schmitt, J. H. M. M., & Voges, W. 1998, A&AS, 132, 155
- Jacoby, G. H., Hunter, D. A., & Christian, C. A. 1984, ApJS, 56, 257
- Johnson, H. L. 1966, ARA&A, 4, 193
- Lada, C. J & Adams, F. C. 1992, ApJ, 393, 278
- Laycock, S., Grindlay, J., van den Berg, M., Zhao, P., Hong, J., Koenig, X., Schlegel, E. M., & Persson, S. E. 2005, ApJ, 634, L53
- Mewe, R., Gronenschild, E. H. B. M., & van den Oord, G. H. J. 1985, A&AS, 62, 197
- Micela, G., Sciortino, S., Kashyap, V., Harnden, F. R., Jr., & Rosner, R. 1996, ApJS, 102, 75
- Mikami, T. & Heck, A. 1982, PASJ, 34, 529
- Muno, M. P., et al. 2003, ApJ, 589, 225
- Muno, M. P., et al. 2004, ApJ, 613, 326
- Nishiyama, S., et al. 2006, ApJ, 638, 839
- Panzer, M. R., Tagliaferri, G., Pasinetti, L., & Antonello 1999, A&A, 348, 161
- Patterson, J. 1998, PASP, 110, 1132
- Predehl, P. & Schmitt, J. H. M. M. 1995, A&A, 293, 889

- Rogel, A. B., Cohn, H. N., & Lugger, P. M. 2008, *ApJ*, 675, 373
- Revnivtsev, M., Sazonov, S., Gilfanov, M., Churazov, E., & Sunyaev, R. 2006, *A&A*, 452, 169
- Sazonov, S., Revnivtsev, M., Gilfanov, M., Churazov, E., & Sunyaev, R. 2006, *A&A*, 450, 117
- Schlegel, D. J., Finkbeiner, D. P., & Davis, M. 1998, *ApJ*, 500, 525
- Schmidt, M. 1968, *ApJ*, 151, 393
- Schmitt, J. H. M. M. & Liefke, C. 2004, *A&A*, 417, 651
- Schwope, A. D., Brunner, H., Buckley, D., Greiner, J., Heyden, K. v. d., Neizvestny, S., Potter, S., & Schwarz, R. 2002, *A&A*, 396, 895
- Sciortino, S., Favata, F., & Micela, G. 1995, *A&A*, 296, 370
- Sidoli, L., Belloni, T., & Mereghetti, S. 2001, *A&A*, 368, 835
- Silva, D. R. & Cornell, M. E. 1992, *ApJS*, 81, 865
- Skrutskie, M. F., et al. 2006, *AJ*, 131, 1163
- Stern, R. A., Schmitt, J. H. M. M., & Kahabka, P. T. 1995, *ApJ*, 448, 683
- Szkody, P., et al. 2004, *AJ*, 128, 1882
- Tagliaferri, G., Cutipoto, G., Pallavicini, R., Randich, S., & Pasquini, L. 1994, *A&A*, 285, 272
- Taylor, A. R., et al. 2003, *AJ*, 125, 3145
- Tinney, C. G., Reid, I. N., & Mould, J. R. 1993, *ApJ*, 414, 254
- Torres-Dodgen, A. V. & Weaver, W. B. 1993, *PASP*, 105, 693
- Vaiana, G. S., Maggio, A., Micela, G., & Sciortino, S. 1992, *Memorie della Societa Astronomica Italiana*, 63, 545
- Verbunt, F., Bunk, W. H., Ritter, H., & Pfeffermann, E. 1997, *A&A*, 327, 602
- Voges, W. 1992, *The ROSAT all-sky X ray survey*, Tech. rep.

Warner, B. 1995, *Cataclysmic variable stars* (Cambridge Astrophysics Series, Cambridge, New York: Cambridge University Press, —c1995)

Wielen, R. 1977, *A&A*, 60, 263

Worrall, D. M., Marshall, F. E., Boldt, E. A., & Swank, J.H. 1982, *ApJ*, 255, 111

Zhang, S. N., Wilson, C. A., Harmon, B. A., Fishman, G. J., Wilson, R. B., Paciesas, W. S., Scott, M., & Rubin, B. C. 1994, *IAU Circ.*, 6046, 1

Zhao, P., Grindlay, J. E., Hong, J. S., Laycock, S., Koenig, X. P., Schlegel, E. M., & van den Berg, M. 2005, *ApJS*, 161, 429

Table 8. CV Detection Constraints for the Five Chandra ObsIDs

| ObsID | Field | CR limit ^a (ksec ⁻¹) | dmax _{32.5} ^b (kpc) | CV _{32.5} ^c | X-detect ^d (%) | XO-detect ^e (%) | ID _{32.5} ^f | Found |
|-------|-------|--|--|---------------------------------|------------------------------|-------------------------------|---------------------------------|-------------------|
| 99 | J1655 | 0.258 | 29.3 | 21.2 | 12.3±0.2 | 2.28±0.03 | 0.48 | 0(1) ^g |
| 737 | G347b | 0.305 | 15.75 | 37.3 | 4.1±0.2 | 0.65±0.03 | 0.24 | 0 |
| 944 | SgrB2 | 0.126 | 14.4 | 65.8 | 3.4±0.2 | 0.05±0.01 | 0.03 | 0 |
| 945 | GalCA | 0.305 | 11.3 | 22.7 | 3.0±0.2 | 0.13±0.02 | 0.03 | 2 |
| 53392 | SgrA★ | 0.061 | 39.5 | 1232.0 | 1.7±0.02 | 0.014±0.002 | 0.17 | 1(1) ^g |
| Total | ... | ... | ... | 1378.8 | ... | ... | 0.95 | 3(5) |

Note. — ^aThe average count rate limit for this observation within 5' of the *Chandra* aimpoint. ^bThe maximum distance we can detect a CV at log(L_x)=32.5. ^cThe number of CVs in the effective volume defined by the Tinney formula for this sky position and d_{max}. ^dThe expected percentage of these CVs detected in X-rays. ^eThe expected percentage of these CVs also detected optically. ^fThe resultant number of CVs we expect to identify in this field. ^gThis field includes one spectroscopically unconfirmed CV, see Table 9.

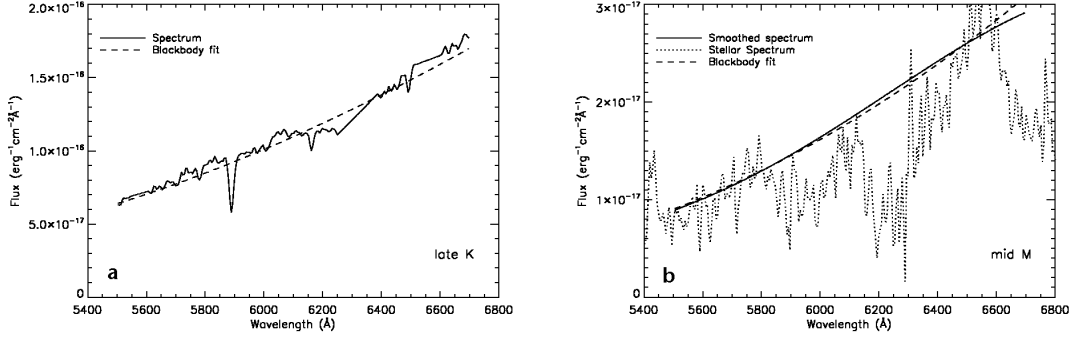


Fig. 1.— Two example fits to spectra from the LDSS2 sample. The panel for the M star (right) also shows the polynomial fit to the spectrum (see text for description) to which the blackbody curve was subsequently fit.

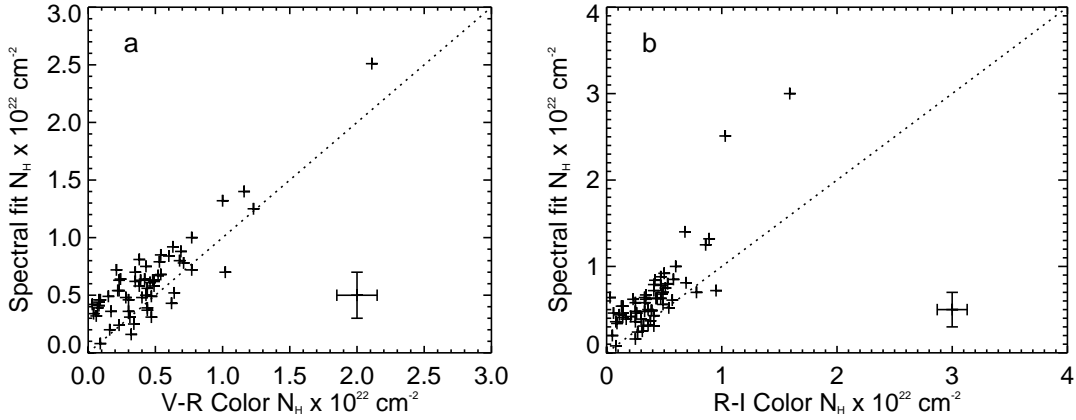


Fig. 2.— Plots of hydrogen column density for all stars with available $V - R$ or $R - I$ photometry in the sample, derived from the spectral fit and color methods detailed in §§ 3.1 and 3.2. Typical error bars and lines of $N_H(\text{Color}) = N_H(\text{Fit})$ (dotted line) are shown for reference.

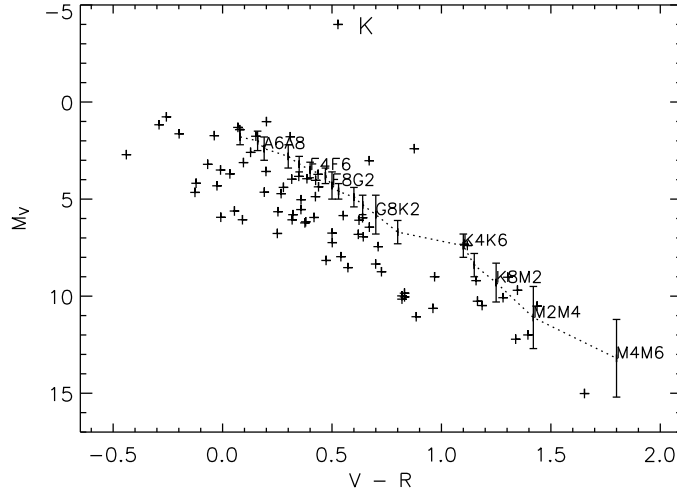


Fig. 3.— A Color-Magnitude diagram of the stars in the LDSS2 sample. We plot $M_V = V - 5 \log(\text{dist}) + 5 - A_V$, and $(V - R)_0 = V - R - 0.781E(B - V)$. The star marked ‘K’ is the K giant in SgrB2, ChOPSJ174642.22–282907.4. The dotted curve and spectral type labels are from Cox (10) and the error bars show the range of M_V for spectral type range plotted.

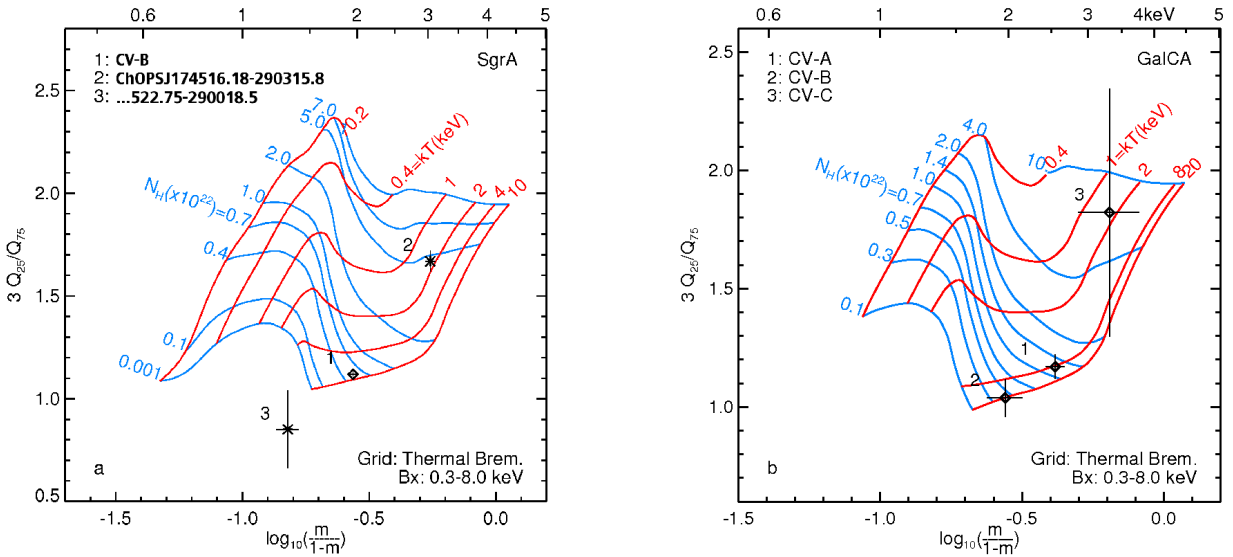


Fig. 4.— Left panel: QCCD plot for ObsID 53392 (SgrA \star) showing the positions of CV-B and non-identified sources from the SgrA \star field with at least 107 counts. Right panel: ObsID 945 (GalCA) showing all three CVs.

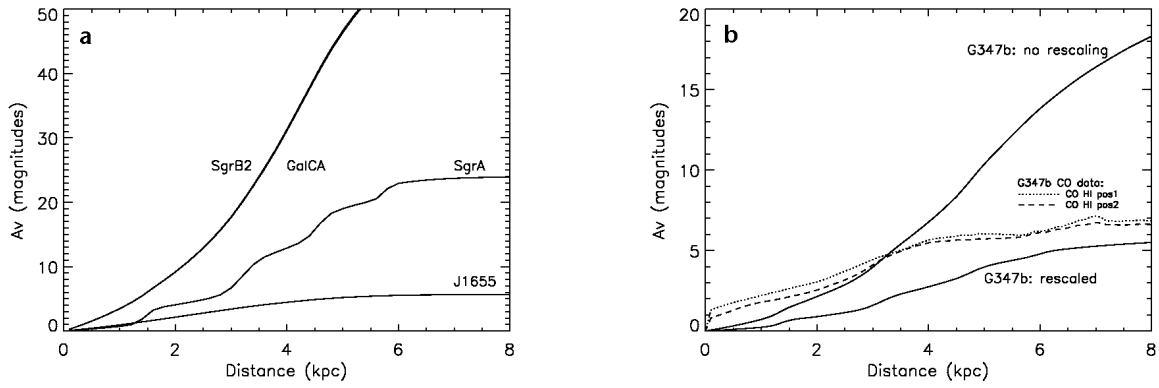


Fig. 5.— Plots of A_V (re-scaled values) versus distance from the model of Drimmel & Spergel (17) for the five *Chandra* fields. For field G347b (right-hand plot) we show the results of both rescaled and non-rescaled A_V versus distance from this paper, and also overplot our own results, as derived from CO+HI observations. See § 3.2 for a description.

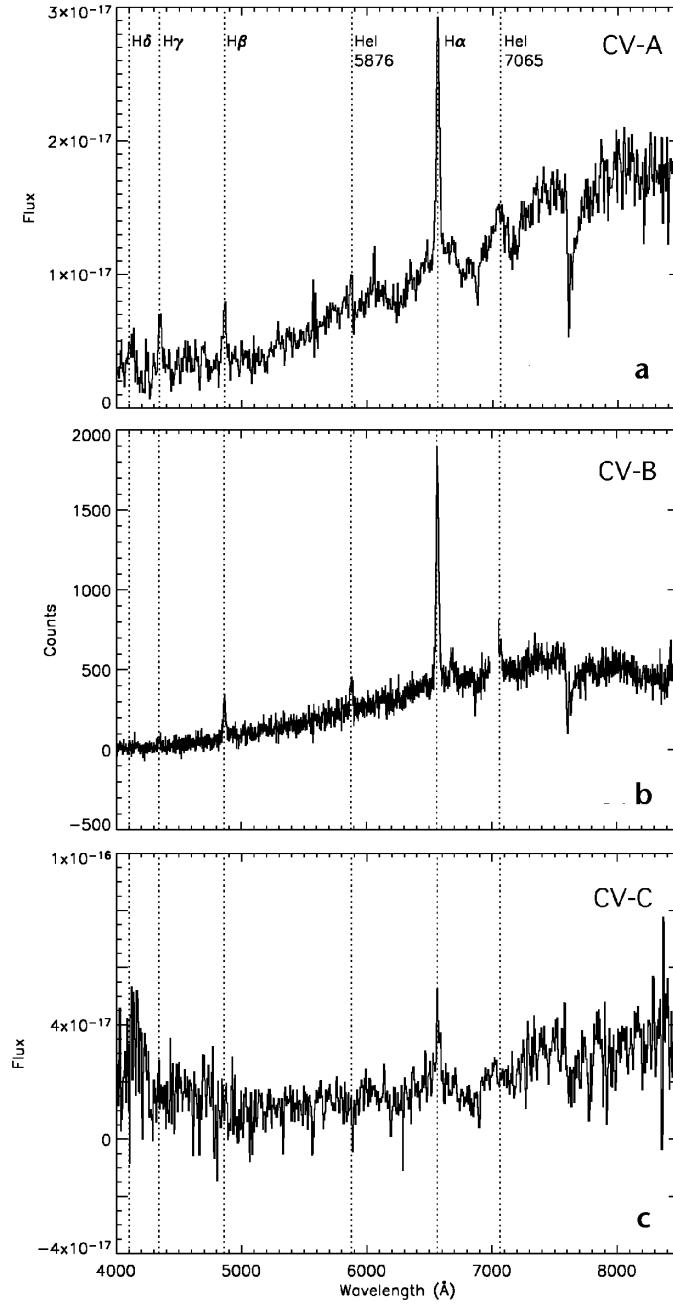


Fig. 6.— The three CVs discovered in the five *Chandra* fields in this paper. The LDSS2 spectra for CV-A and CV-C have y-axis units $\text{ergs s}^{-1} \text{cm}^{-2} \text{Å}$. The IMACS spectrum for CV-B was not flux calibrated and has y-axis units in raw counts. The region 6990–7500Å has been removed from CV-B as it covers a CCD chip gap.

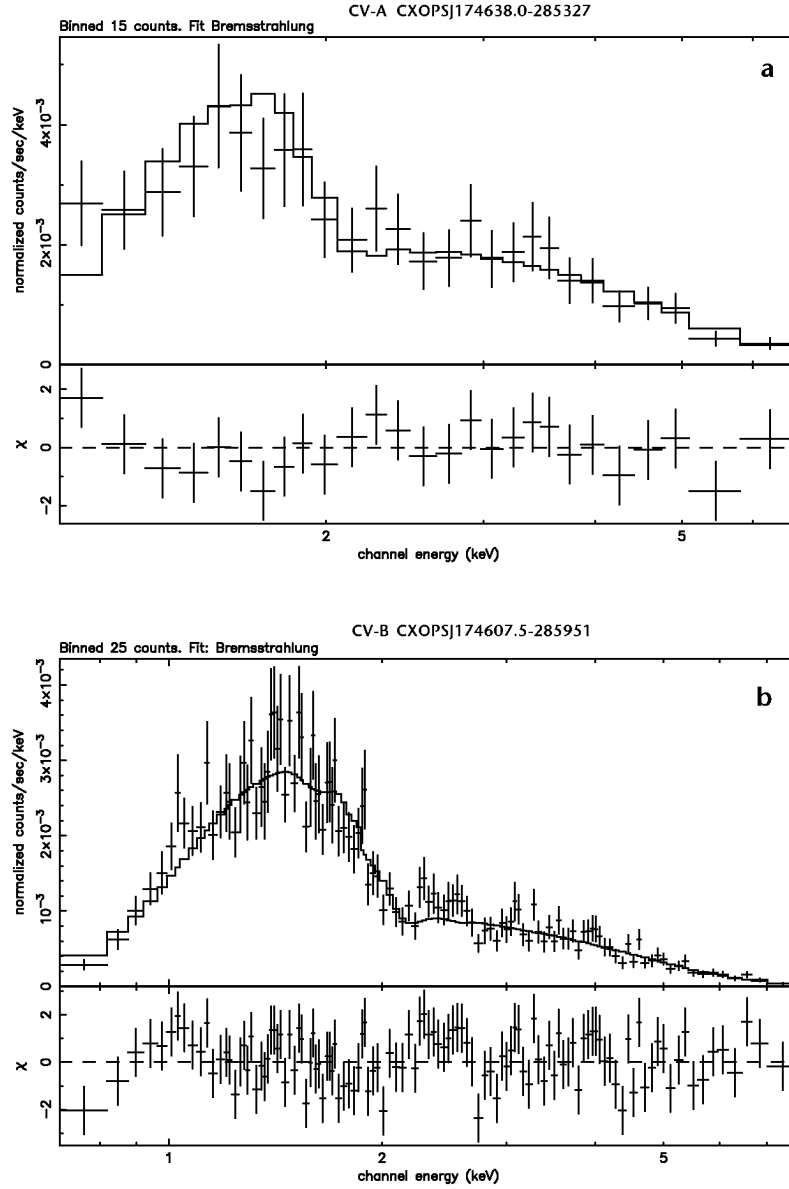


Fig. 7.— XSPEC fits to the X-ray data for the CV-A and CV-B detected in this survey. Upper spectrum, CV-A: 438 ± 22 net counts (B_X band), lower spectrum, CV-B: 3539 ± 63 net counts. We plot the spectrum plus fit, and in the lower panel in each case the residuals of the spectrum divided by the errors.

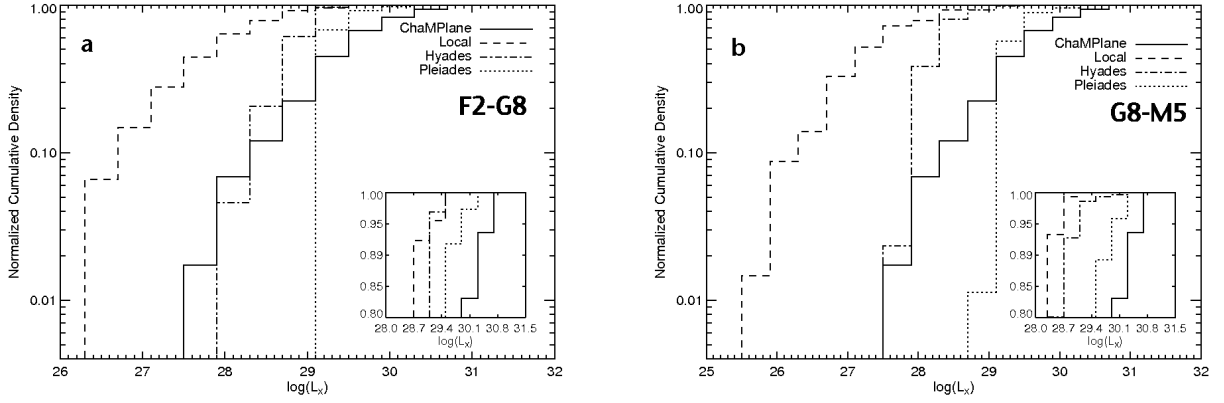


Fig. 8.— X-ray luminosity functions of our stellar coronal sample, $1/V_{max}$ corrected. We divide our sample into stars from type F2–G8 (58 stars, left panel) and G8–M5 (48 stars, right panel). Inset in each Figure is a zoomed in portion of the top part of the plot. We overplot comparison stellar samples from the a local sample, plus the Hyades and Pleiades.

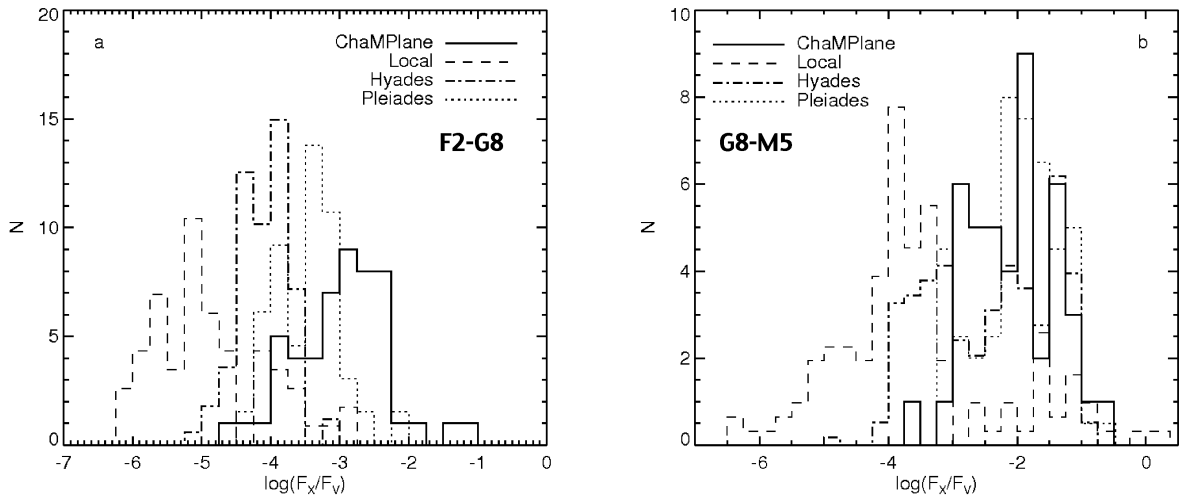


Fig. 9.— Histograms by spectral type grouping (same as Figure 7) of the X-ray to optical flux ratio of our stellar sample, overplotted with data from the studies of Schmitt & Liefke (51) (dashed) and the Hyades and Pleiades samples of Stern et al. (57) and Micela et al. (38). We classify 62–77% of our M stars as dMe from their $H\alpha$ emission.

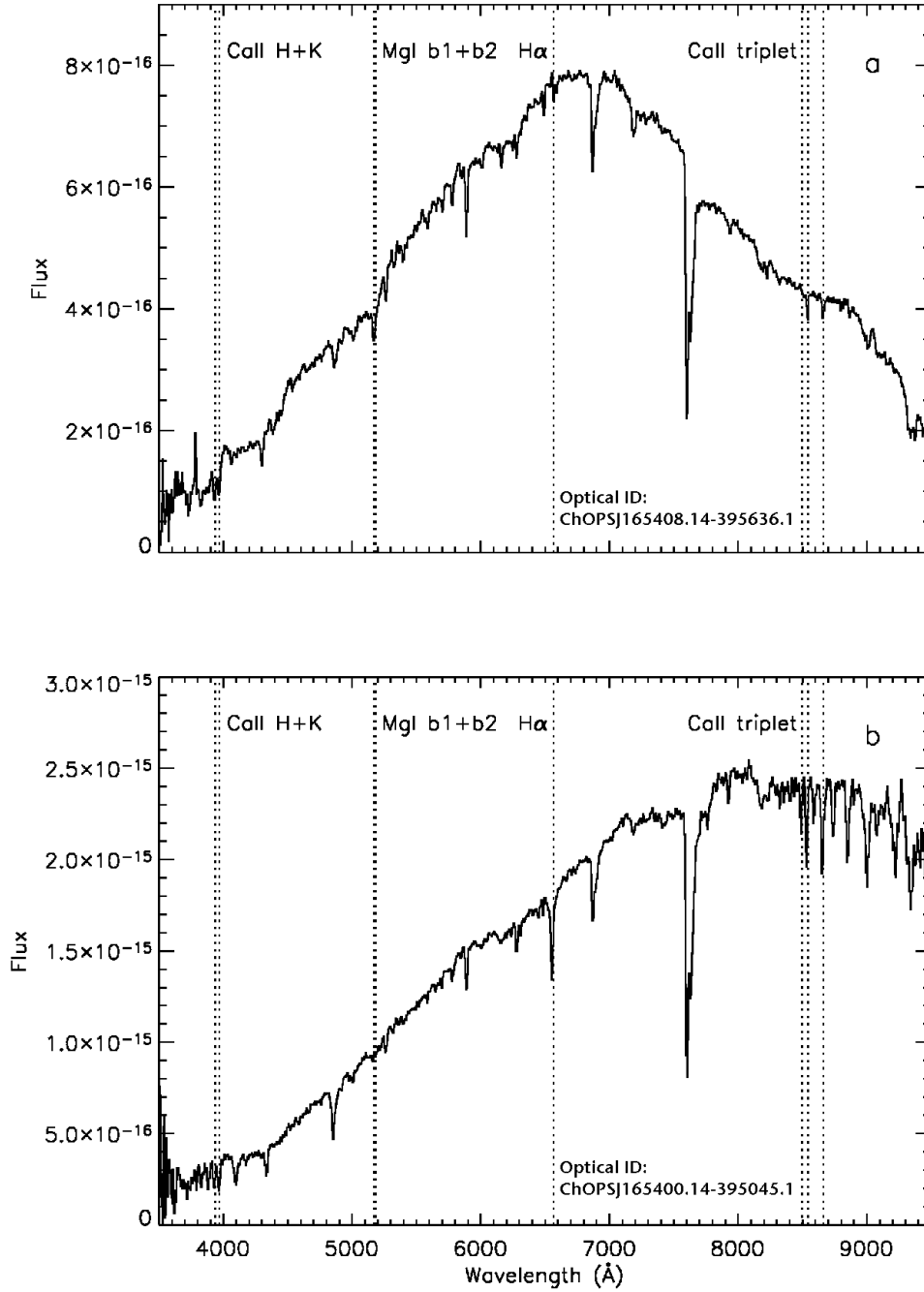


Fig. 10.— Upper spectrum: the qLMXB candidate found in our LDSS2 sample. Lower spectrum: GRO J1655 –40 as observed by LDSS2 from our June 2002 observing run. The flux scale has units: $\text{ergs s}^{-1} \text{cm}^{-2} \text{Å}^{-1}$. Important spectral lines are marked on the spectra for reference. The strongest spectral feature at $\lambda 7600$ is telluric absorption by the Earth’s atmosphere.

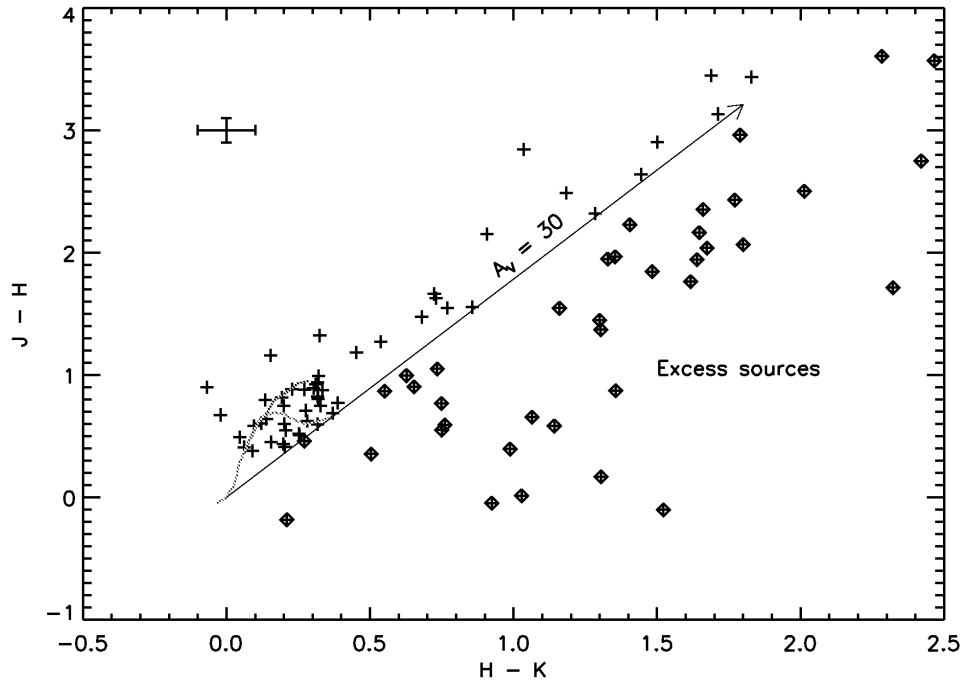


Fig. 11.— $J - H$ versus $H - K_S$ plot of 2MASS sources matched with ChaMPlane sources in this paper. Overlaid is the locus of dwarf and giant stars (giant stars are redder) from Bessell & Brett (5). The arrow represents an extinction of $A_V=30$ using the extinction relation of Nishiyama et al. (42). Sources marked with diamond points are candidate excess sources/young stars. A typical error bar is shown, upper left.